GluN2C/D-containing NMDA receptors enhance temporal summation and increase sound-evoked and spontaneous firing in the inferior colliculus

Abbreviated title: GluN2C/D-containing NMDARs in the IC

Audrey C. Drotos[1], Rachel L. Zarb[1], Victoria Booth[3,4], Michael T. Roberts[1,2,]*

1. Kresge Hearing Research Institute, Department of Otolaryngology – Head and Neck Surgery, University of Michigan, Ann Arbor, Michigan 48109
2. Department of Molecular and Integrative Physiology, University of Michigan, Ann Arbor, Michigan 48109
3. Department of Mathematics, University of Michigan, Ann Arbor, Michigan 48109
4. Department of Anesthesiology, University of Michigan, Ann Arbor, Michigan 48109

*Corresponding author: microb@umich.edu

Number of pages: 51
Number of figures: 9
Number of tables: 2
Number of words in abstract: 234
Number of words in introduction: 599
Number of words in discussion: 1398

Conflict of Interest Statement: The authors declare no competing financial interests.

Acknowledgements: The authors would like to thank Yoani Herrera, Marina Silveira, Pierre Apostolides, Marie Walicki, Will Birdsong, and Kelly Sovacool for helpful discussions and advice. This work was supported by a Rackham Graduate Student Research Grant (ACD), the National Science Foundation Graduate Research Fellowship Program under Grant No. DGE 1256260

(ACD), the National Institutes of Health Grant R01 DC018284 (MTR), and the National Institutes of Health Grant F31 DC021344 (ACD).

Author contributions: ACD and MTR conceived of the study and designed experiments. ACD, VB, and RLZ conducted experiments. ACD analyzed data, prepared figures, and prepared the initial draft of the manuscript. ACD and MTR revised the manuscript, and all authors approved the submitted version.

Significance statement

NMDA receptors are critical components of most glutamatergic circuits in the brain, and the diversity of NMDA receptor subtypes yields receptors with a variety of functions. We found that many neurons in the auditory midbrain express GluN2C and/or GluN2D NMDA receptor subunits, which are less sensitive to Mg^{2+} block than the more commonly expressed GluN2A/B subunits. We showed that GluN2C/D-containing receptors conducted current at resting membrane potential and enhanced temporal summation of synaptic inputs. In a model, we show that GluN2C/D-containing receptors provide additive gain for input-output functions driven by trains of synaptic inputs. In line with this, we found that blocking GluN2C/D-containing NMDA receptors in vivo decreased both spontaneous firing rates and firing evoked by amplitude-modulated sounds.

Abstract

Along the ascending auditory pathway, there is a broad shift from temporal coding, which is common in the lower auditory brainstem, to rate coding, which predominates in auditory cortex. This temporal-to-rate transition is particularly prominent in the inferior colliculus (IC), the midbrain hub of the auditory system, but the mechanisms that govern how individual IC neurons integrate information across time remain largely unknown. Here, we report the widespread expression of *Glun2c* and *Glun2d* mRNA in IC neurons. GluN2C/D-containing NMDA receptors are relatively insensitive to voltage-dependent Mg^{2+} block, and thus can conduct current at resting membrane potential. Using in situ hybridization and pharmacology, we show that VIP neurons in the IC express GluN2D-containing NMDA receptors that are activatable by commissural inputs from the contralateral IC. In addition, GluN2C/D-containing receptors have much slower kinetics than other NMDA receptors, and we found that GluN2D-containing receptors facilitate temporal summation of synaptic inputs in VIP neurons. In a model neuron, we show that a GluN2C/D-like conductance interacts with the passive membrane properties of the neuron to alter temporal and rate coding of stimulus trains. Consistent with this, we show in vivo that blocking GluN2C/D-containing receptors decreases both the spontaneous firing rate and the overall firing rate elicited by amplitude-modulated (AM) sounds in many IC neurons. These results suggest that GluN2C/D-containing NMDA receptors influence rate coding for auditory stimuli in the IC by facilitating the temporal integration of synaptic inputs.

69 **Introduction**

70 The inferior colliculus (IC) in the midbrain plays a critical role in auditory processing,
71 functioning as a hub of integration in the auditory pathway (Adams, 1979; Oliver and Huerta,
72 1992) and as a site where phase-locked ascending inputs are transformed into a firing rate code
73 (Hewitt and Meddis, 1994; Joris et al., 2004). However, the cellular and circuit mechanisms that
74 govern how IC neurons integrate synaptic inputs and convert temporal to rate codes remain
75 largely unknown. In other brain regions, the slow kinetics of NMDA receptors (NMDARs) can
76 play a critical role in temporal integration of synaptic inputs (D'Angelo et al., 1995; Lo et al.,
77 2013). Intriguingly, previous studies have found that many IC neurons express NMDARs that are
78 activated at resting membrane potential (Kelly and Zhang, 2002; Ma et al., 2002; Wu, 2004;
79 Oberle et al., 2022). In line with this previous work, we recently found in adult mice that
80 optogenetic stimulation of commissural inputs elicited excitatory postsynaptic potentials
81 (EPSPs) in IC VIP neurons that had a significant contribution from NMDARs at resting membrane
82 potential (Goyer et al., 2019).

83 These results suggest that NMDARs that conduct current at resting membrane potential
84 are a common feature of IC circuits, but this is unusual. At most glutamatergic synapses,
85 activation of AMPARs is required to depolarize the membrane potential and remove voltage-
86 dependent Mg^{2+} block of NMDARs, allowing NMDARs to contribute to the response. One
87 potential explanation for this phenomenon is that NMDARs in IC neurons may be less sensitive
88 to Mg^{2+} block due to their subunit composition (Paoletti et al., 2013). NMDARs are
89 heterotetramers comprised of two obligatory GluN1 subunits and a combination of GluN2(A-D)
90 and/or GluN3(A-B) subunits (Traynelis et al., 2010). A residue in the GluN2 subunit confers Mg^{2+}
91 sensitivity (Monyer et al., 1992; Siegler Retchless et al., 2012), with GluN2C/D subunit-
92 containing receptors being much less sensitive to Mg^{2+} block than GluN2A/B subunit-containing
93 receptors. Inclusion of GluN2C/D subunits in NMDARs thus gives rise to receptors with
94 significant currents at resting membrane potential, as has been demonstrated in the mouse
95 barrel cortex (Binshtok et al., 2006).

96 In addition to their differences in Mg^{2+} sensitivity, NMDARs containing GluN2C or
97 GluN2D subunits have slower kinetics than NMDARs with GluN2A or GluN2B subunits (Paoletti

98 et al., 2013). These slow kinetics can expand the time window for temporal summation of
99 synaptic inputs, as seen in neocortex, where GluN2C/D-containing receptors enable pyramidal
100 neurons to integrate intracortical inputs over broader time windows than GluN2A/B-containing
101 receptors (Kumar and Huguenard, 2003).
102 Here, we tested whether GluN2C/D-containing NMDARs mediate NMDAR currents in
103 the IC and the role of these receptors in synaptic integration and sound processing. We found
104 that IC VIP neurons, a class of excitatory principal neurons (Goyer et al., 2019), express
105 NMDARs that activate at resting potential. We show that VIP neurons express *Glun2d* mRNA
106 and that many other IC neurons express *Glun2c* and/or *Glun2d* mRNA, pointing to a prominent
107 role for GluN2C/D-containing NMDARs in the IC. NMDAR-mediated responses in VIP neurons
108 were sensitive to GluN2C/D-specific pharmacology and were elicited by commissural inputs
109 from the contralateral IC. Additionally, GluN2C/D-specific antagonists decreased temporal
110 summation of commissural inputs in VIP neurons. In a model neuron, addition of an NMDAR-
111 like conductance lacking Mg^{2+} sensitivity altered temporal and rate coding. In line with this,
112 during in vivo recordings from awake mice, local infusion of a GluN2C/D-specific antagonist
113 decreased spontaneous and sound-evoked firing rates in many IC neurons. Overall, these
114 results provide a molecular mechanism for the presence of NMDAR currents at resting potential
115 in many IC neurons and show that the widespread expression of GluN2C/D subunits in the IC
116 influences sound processing.
117

118 **Materials and Methods**

119 **Animals**

120 All experiments were approved by the University of Michigan Institutional Animal Care
121 and Use Committee and were in accordance with NIH guidelines for the care and use of
122 laboratory animals. Animals were kept on a 12-hour day/night cycle with ad libitum access to
123 food and water. To visualize VIP neurons, VIP-IRES-Cre mice (*Vip*$^{TM1(cre)Zjh}$/J, Jackson Laboratory,
124 stock #010908) (Taniguchi et al., 2011) were crossed with Ai14 reporter mice (B6.Cg-
125 *Gt(ROSA)26Sor*$^{TM\ 14(CAG–tdTomato)Hze}$/J, Jackson Laboratory, stock #007914) (Madisen et al., 2010)
126 so that the fluorescent protein tdTomato was expressed in VIP neurons (Beebe et al., 2022).

127 Since mice on the C57BL/6J background undergo age-related hearing loss after 3 months of age
128 (Zheng et al., 1999), all experiments were performed on mice between postnatal days (P)30 –
129 66.
130
131 **Brain slice preparation**
132 Whole-cell patch-clamp recordings were performed in acutely prepared IC slices from
133 VIP-IRES-Cre x Ai14 mice. Male (n = 18) and female (n = 15) mice aged P30 – P66 were used.
134 Mice were deeply anesthetized with isoflurane and then rapidly decapitated. The brain was
135 removed and the IC was dissected in 34 °C artificial cerebrospinal (ACSF) solution containing (in
136 mM): 125 NaCl, 12.5 glucose, 25 $NaHCO_3$, 3 KCl, 1.25 NaH_2PO_4, 1.5 $CaCl_2$, 1 $MgSO_4$, 3 sodium
137 pyruvate and 0.40 L-ascorbic acid (Acros Organics), bubbled with 5% CO_2 in 95% O_2. 200 µm
138 coronal slices containing the IC were cut using a vibrating microtome (VT1200S, Leica
139 Biosystems). Slices were incubated at 34 °C for 30 min in ACSF bubbled with 5% CO_2 in 95% O_2
140 and then placed at room temperature for at least 30 min before initiating recordings.
141 Recordings were targeted to tdTomato-expressing VIP neurons in the central nucleus of the IC
142 using a Nikon FN1 or Olympus BX51 microscope. All chemicals were obtained from Thermo
143 Fisher Scientific unless otherwise noted.
144
145 **Voltage-clamp electrophysiological recordings**
146 Slices were placed in a recording chamber and continuously perfused at a rate of ~2
147 ml/min with 34 °C ACSF bubbled in 5% CO_2/95% O_2. Whole-cell voltage-clamp recordings were
148 performed with an Axopatch 200A patch clamp amplifier (Axon Instruments). For each
149 recording, series resistance compensation was performed using 80% prediction and 80%
150 correction, and whole cell capacitance was compensated. Series resistance for all neurons
151 included in this study was <15 MΩ. Data were low-pass filtered at 10 kHz, sampled at 50 kHz
152 with a National Instruments PCIe-6343 data acquisition board, and acquired using custom
153 software written in Igor Pro (Sutter Instrument). Recording pipettes were pulled from
154 borosilicate glass capillaries (outer diameter 1.5 mm, inner diameter 0.86 mm, Sutter
155 Instrument) with a P-1000 microelectrode puller (Sutter Instrument) and filled with an internal

156 solution containing (in mM): 115 CsOH, 115 D-gluconic acid, 7.76 CsCl, 0.5 EGTA, 10 HEPES, 10
157 Na_2 phosphocreatine, 4 MgATP, 0.3 NaGTP, supplemented with 0.1% biocytin (w/v), pH
158 adjusted to 7.4 with CsOH and osmolality to 290 mmol/kg with sucrose. Voltage clamp
159 recordings were not corrected for the liquid junction potential. All electrophysiological
160 recordings were targeted to neurons in the central nucleus of the IC, but it is possible a small
161 number of recordings were performed in the dorsal cortex of the IC.

162 To apply glutamate puffs to brain slices, we pulled puffer pipettes from borosilicate
163 glass (outer diameter 1.5 mm, inner diameter 0.86 mm, Sutter Instrument) to a resistance of
164 3.5 – 5.0 MΩ using a P-1000 microelectrode puller and filled them with 300 μM glutamate
165 (Sigma, # G5889) dissolved in a vehicle solution containing (in mM): 125 NaCl, 3 KCl, 12.5
166 glucose and 3 HEPES. The solution was balanced to a pH of 7.40 with NaOH. Puffer pipettes
167 were connected to a pressure ejection system built based on the OpenSpritzer design (Forman
168 et al., 2017). The tips of puffer pipettes were placed near the soma of the recorded cell, and 10
169 ms puffs were presented either 10 ms or 30 ms apart (30 ms for drug conditions) with 5 puffs
170 presented per condition. Puffs containing only the vehicle solution did not elicit any response in
171 the neurons tested (data not shown).

172 To examine whether NMDAR activation in VIP neurons at resting membrane potential is
173 mediated by NMDARs containing GluN2C/D subunits, we performed whole-cell patch-clamp
174 recordings targeted to VIP neurons as described above. To isolate the contribution of NMDARs,
175 recordings were performed in the presence of 10 μM NBQX, an AMPAR antagonist. Glutamate
176 was puffed onto VIP neurons during bath application of 1.5 μM PPDA (Hello Bio, #HB0531), a
177 GluN2C/D specific antagonist (Lozovaya et al., 2004; Li et al., 2020; Jing et al., 2022), or 20 μM
178 CIQ (Hello Bio, HB0197), a GluN2C/D specific positive allosteric modulator (Mullasseril et al.,
179 2010; Feng et al., 2014; Zhang et al., 2014; Nouhi et al., 2018; Liu et al., 2021). The
180 concentrations of PPDA and CIQ used throughout this study are based on previous studies that
181 used PPDA (Lozovaya et al., 2004; Li et al., 2020; Jing et al., 2022) or CIQ (Feng et al., 2014,
182 2014; Nouhi et al., 2018; Liu et al., 2021). All drugs were washed in for 10 minutes before
183 testing how the drugs affected responses to glutamate puffs.

184 CIQ and PPDA were prepared in 0.04% and 0.003% DMSO (volume/volume),
185 respectively. To test for vehicle effects, we performed control experiments where puff-elicited
186 EPSCs were compared between control and DMSO (vehicle) conditions. No differences in puff-
187 elicited EPSCs were found after DMSO wash-in (Linear mixed model tests: amplitude, $\beta = -5.96$,
188 $p = 0.42$, CI [-20.2, 8.28], halfwidth, $\beta = 7.50$, $p = 0.36$, CI [-8.36, 23.37], rise time, $\beta = 13.87$, $p =$
189 0.53, CI [-30.16, 57.91], decay tau, $\beta = -115.62$, $p = 0.20$, CI [-281.84, 50.60]).
190
191 **Mg^{2+}-free voltage-clamp recordings**
192 To determine what proportion of NMDARs on VIP neurons contain GluN2C/D subunits
193 vs GluN2A/B subunits, we performed whole-cell patch-clamp recordings targeted to VIP
194 neurons as described above, except immediately prior to patching brain slices were transferred
195 to a Mg^{2+}-free ACSF solution containing (in mM): 125 NaCl, 12.5 glucose, 25 $NaHCO_3$, 3 KCl, 1.25
196 NaH_2PO_4, 2.5 $CaCl_2$, 0 $MgSO_4$, 3 sodium pyruvate and 0.40 L-ascorbic acid (Acros Organics),
197 bubbled with 5% CO_2 in 95% O_2. To isolate the contribution of NMDARs, recordings were
198 performed in the presence of 10 μM NBQX. To determine whether GluN2A/B-containing
199 NMDARs were present on VIP neurons, we first performed control glutamate puffs and then
200 puffs after bath application of 1.5 μM PPDA, followed by puffs after bath application of 100 μM
201 D-AP5, a broad NMDAR antagonist. All drugs were washed in for 10 minutes before testing how
202 the drugs affected the response to glutamate puffs.
203
204 **Intracranial virus injections**
205 Mice used for intracranial injections of recombinant adeno-associated viruses (AAVs)
206 were between ages P26 – 39. Mice were anesthetized with 1-3% isoflurane (Piramal Critical
207 Care, # NDC 66794-017-25) and body temperature was maintained using a homeothermic
208 heating pad. To minimize postoperative pain, an injection of carprofen (5 mg/kg, CarproJect,
209 Henry Schein Animal Health) was administered subcutaneously. The scalp was shaved using
210 scissors and an incision was made along the midline of the scalp to expose the skull. The
211 injection site was identified using previously validated coordinates for the IC (all coordinates are
212 relative to the skull surface at lambda; in μm: 900 caudal, 1000-1250 lateral, 1850 deep, with

213 two penetrations, one for each lateral coordinate) and a craniotomy was drilled using a
214 micromotor drill (K.1050, Foredom Electric Co.) with a 0.5 mm burr (Fine Science Tools). Glass
215 injection pipettes were pulled from capillary glass (Drummond Scientific Company) using a P-
216 1000 microelectrode puller (Sutter Instruments) and cut on a diagonal for a beveled opening of
217 ~20 μm. Pipettes were first backloaded with mineral oil and then front filled with
218 AAV1.Syn.Chronos-GFP.WPRE.bGH (Addgene, #59170-AAV1, titer: 1.4e13, 2.2e13),
219 AAV5.Syn.Chronos-GFP.WPRE.bGH (Addgene, #59170-AAV5, titer: 5.3e12), or
220 AAV9.Syn.Chronos-GFP-WPRE.bGH (University of North Carolina Vector Core, Addgene plasmid
221 #59170, titer: 4.5e12) (Klapoetke et al., 2014). The virus was injected using a NanoJect III
222 nanoliter injector (Drummond Scientific Company) connected to an MP-285 micromanipulator
223 (Sutter Instrument). IC injections were made in two penetrations along the medial-lateral axis
224 that were 250 µm apart, and viral deposits were made at 250 µm intervals along the ventral-
225 dorsal axis for a total of 4 deposits at the more medial site and 3 deposits at the more lateral
226 site. 20 nL of virus was deposited per injection, for a total of 150 nL virus injected per IC. After
227 the injections were completed, the scalp was closed either by suturing with Ethilon 6-0 (0.7
228 metric) nylon sutures (Ethicon USA, LLC) or applying Vetbond (3M, #1469SB) on top of the
229 closed incision. For postoperative analgesia, 0.5 mL of 2% Lidocaine hydrochloride jelly (Akorn
230 Inc) was placed on top of the sutures. Mice were observed for 1 hr for indications of pain or
231 distress and then returned to the vivarium once they were ambulatory. Mice were monitored
232 daily until sutures fell out and the wound was completely healed. Sutures remaining on the 10th
233 post-operative day were manually removed.
234
235 **Current-clamp recordings**
236 Slices were placed in a recording chamber and continuously perfused at a rate of ~2
237 ml/min with 34 °C oxygenated ACSF. Whole-cell current-clamp recordings were performed with
238 a BVC-700A patch clamp amplifier (Dagan Corporation). Data were low-pass filtered at 10 kHz,
239 sampled at 50 kHz with a National Instruments PCIe-6343 data acquisition board, and acquired
240 using custom software written in Igor Pro. Recording pipettes were pulled from borosilicate
241 glass pipettes (outer diameter 1.5 mm, inner diameter 0.86 mm, Sutter Instrument) with a P-

242 1000 microelectrode puller (Sutter Instrument) and filled with an internal solution containing
243 (in mM): 115 K-gluconate, 7.73 KCl, 0.5 EGTA, 10 HEPES, 10 Na_2phosphocreatine, 4 MgATP, 0.3
244 NaGTP, supplemented with 0.1% biocytin (w/v), pH adjusted to 7.3 with KOH and osmolality to
245 290 mmol/kg with sucrose. All membrane potentials for current-clamp recordings were
246 corrected for an 11 mV liquid junction potential.
247
248 **Optogenetics**
249 Current-clamp recordings were conducted 2 – 4 weeks after virus injections to allow
250 time for Chronos expression. Recordings were conducted as described above, except that brain
251 slices were prepared and incubated under red light to limit Chronos activation. To verify the
252 virus injection location in IC injections, fluorescence was visualized under the microscope
253 during the recording session. Recordings were targeted to neurons contralateral to the
254 injection site.
255 Chronos was activated using 2-10 ms pulses of 470 nm light emitted by a blue LED
256 coupled to the epi-fluorescence port of the microscope and delivered to the slice through a
257 0.80 NA 40x water immersion objective. Blue light flashes illuminated the entire field of the
258 0.80 NA 40x objective, corresponding to optical power densities of 6 to 48 mW/mm^2. Optical
259 power was set using the minimum stimulation needed to elicit an EPSP from the recorded
260 neuron. Recording sweeps with light flashes were repeated 10-30 times with 10 ms between
261 light flashes.
262
263 **RNAScope in situ hybridization**
264 Fluorescent in situ hybridization was performed using the RNAscope Multiplex
265 Fluorescent V2 Assay (Advanced Cell Diagnostics, catalog # 320850). Our methods were
266 identical to those previously described (Beebe et al., 2022) and followed manufacturer
267 recommendations (Wang et al., 2012). Briefly, one male (P47) and two female (P45) mice were
268 deeply anesthetized with isoflurane and brains were rapidly removed and frozen on dry ice.
269 Brains were placed in a -80 °C freezer until the day of slicing. Prior to slicing, brains were
270 equilibrated at -20 °C for 1 hour. Brains were sliced into 15 µM sections using a cryostat at -20

271 °C and sections were mounted on Superfrost Plus slides (Fisher Scientific, catalog # 22037246).
272 For each mouse, five representative sections were chosen spanning the caudal—rostral axis.
273 Sections were fixed using 10% neutral buffered formalin (Sigma-Aldrich, catalog # HT501128)
274 and dehydrated using repeated washes in 50%-100% ethanol. Slides were dried using a Kim
275 wipe and a hydrophobic barrier was drawn around each section. Slices were next incubated in
276 hydrogen peroxide for 10 minutes at room temperature, followed by application of Protease IV
277 for 30 minutes. Probes for *tdTomato*, *Glun2c*, and *Glun2d* (all experimental slices except
278 controls; Advanced Cell Diagnostics catalog #: 317041-C3, 445581-C2, 425951, respectively),
279 along with positive and negative controls (one control slice each), were applied to slices and
280 incubated for 2 hours at 40 °C. The probes were amplified three times for 30 minutes each time
281 at 40 °C using AMP 1-3. The signal was developed using the HRP for each channel and then opal
282 dyes diluted at 1:1000 were assigned for each channel: *tdTomato* was assigned to Opal 690
283 (Akoya Bioscience, catalog # FP1497001KT), *Glun2c* was assigned to Opal 570 (Akoya
284 Bioscience, catalog # FP1488001KT), and *Glun2d* was assigned to Opal 520 (Akoya Bioscience,
285 catalog # FP1487001KT). Slices were counterstained with DAPI and coverslipped with ProLong
286 Gold antifade mountant (Fisher Scientific, catalog # P36934). Slices were imaged within 1 week
287 of performing the assay using the 0.75 NA 20X objective on a Leica TCS SP8 laser scanning
288 confocal microscope (Leica Microsystems) at 2 µm depth intervals. Emission wavelengths were
289 adjusted for each channel as follows: DAPI (405 nm laser, 410-441 nm), *Glun2d* (488 nm laser,
290 491-528 nm), *Glun2c* (552 nm laser, 565-583 nm), *tdTomato* (638 nm laser, 690-727 nm).
291 Co-localization of *Glun2c* and *Glun2d* in *tdTomato*-positive neurons was quantified
292 manually using Neurolucida 360 (MBF Bioscience). One side of the IC (left or right) was selected
293 randomly for quantification in each slice. *tdTomato*-positive neurons were first identified by
294 placing a marker on top of the cell, and then *Glun2c* and *Glun2d* fluorescence was quantified
295 separately for each marked cell. Cells were considered positive for *Glun2c* or *Glun2d* when one
296 or more puncta co-localized with the *tdTomato* fluorescence. All *tdTomato*-positive neurons
297 counted co-labeled with DAPI.
298 Subdivisions of the IC were determined for each IC slice used in the above analysis by
299 comparison to a reference series of sections from a control C57BL/6J mouse aged P49 that

300 were immunolabeled for GAD67 and GlyT2. This pattern of labeling is routinely used to identify
301 IC subdivisions (Choy Buentello et al., 2015; Beebe and Schofield, 2021), including in our
302 previous studies (Silveira et al., 2020; Anair et al., 2022).
303
304 **Analysis of electrophysiological recordings**
305 Amplitude, halfwidth, rise time, and decay time constant measurements were made
306 using custom algorithms in Igor Pro 8. Voltage-clamp data were low-pass filtered at 3 kHz prior
307 to analysis, except for the commissural optogenetic experiment (**Figure 5**), where data were
308 low-pass filtered at 1 kHz and the following function was fit to each response, which was then
309 analyzed:

310 $$f(x) = y_0 + amp\left(1 - e^{\frac{-(x-x_0)}{\tau_{rise}}}\right) * e^{\frac{-(x-x_0)}{\tau_{decay}}}$$

311
312 For the temporal summation experiment (**Figure 6**), individual sweeps from each condition
313 were averaged and measurements were made from the average waveform.
314
315 **Headbar implantation**
316 Mice used for in vivo experiments were either CBA/CaJ (N = 1 female, age at recording =
317 P51), CBA/C57 (N = 7; 4 females, age range at recording = P81-127), or VIPxAi14 (N = 2
318 females, ages 50, 53 at recording). Mice were anesthetized with 1-3% isoflurane (Piramal
319 Critical Care, # NDC 66794-017-25) and body temperature was maintained using a
320 homeothermic heating pad. To minimize postoperative pain, injections of carprofen (5 mg/kg,
321 CarproJect, Henry Schein Animal Health) and buprenorphine (0.1 mg/kg) were administered
322 subcutaneously. The scalp was shaved using scissors and an incision was made along the
323 midline of the scalp to expose the skull. The inferior colliculus was identified using previously
324 validated coordinates for either the IC (all coordinates are relative to lambda; in μm: 900
325 caudal, 1125 lateral) and marked using a surgical marker. The skull was numbed with 0.2 mL
326 bupivacaine and then the periosteum was removed using a scalpel and the skull was scored.
327 After the skull was prepped, a thin layer of Metabond (C&B Metabond from Parkell, cat #s

328 S398, S399, S371) was applied using a fine paintbrush and allowed to dry for 10 minutes. A thin
329 layer of dental acrylic (Henry Schein, Inc., # 1259208 and # 1250143) was then applied on top of
330 the Metabond, and then dental acrylic was applied to a custom-designed headbar which was
331 placed on the skull. Layers of dental acrylic were added to the headbar to secure it to the skull,
332 and then the opening above the IC was filled with silicon elastomer (Smooth-On Inc. Body
333 Double FAST) and secured with a thin strip of dental acrylic. Mice were observed for 1 hr for
334 indications of pain or distress and then returned to the vivarium once they were ambulatory.
335 For postoperative analgesia, an additional injection of buprenorphine (0.1 mg/kg) was given the
336 day following the surgery, and mice were monitored daily for 7 days.
337
338 **In vivo electrophysiological recordings with drug delivery**
339 Mice were allowed to recover for 3 days following headbar implantation and then began
340 habituation to the head fixation setup, which consisted of 1 day of handling within the cage and
341 3-5 days of head fixation in the sound booth for increasing time duration (10 minutes, 20
342 minutes, 40 minutes, 60 minutes, 80 minutes). After the habituation period, a craniotomy was
343 surgically drilled above the left IC using the procedures outlined here under "intracranial virus
344 injections". Mice were allowed to recover for 1 hour, and then placed in the head fixation
345 setup. For drug delivery, drug delivery pipettes were pulled identically to those used for virus
346 injection in the "intracranial virus injections" section. Drug delivery pipettes were affixed at a
347 ~30 degree angle to recording pipettes (pulled identically to as described in "current clamp
348 recordings") using melted beeswax (Fisher Scientific, # S25192A) such that the tips of both
349 pipettes were 50-200 µm apart. The drug delivery pipette was backfilled with 20 µM DQP
350 (Tocris, #4491) diluted in the in vivo internal solution (in mM, 1.5 $CaCl_2$, 135 NaCl, 1 $MgCl_2$, 5.4
351 KCl, 5 HEPES) and connected to FEP tubing which was attached to a 10 µL Hamilton syringe in a
352 syringe pump (World Precision Instruments Micro4 MicroSyringe Pump Controller). The
353 recording pipette was backfilled with in vivo internal solution and advanced into the brain
354 slowly using an MP-285 micromanipulator (Sutter Instruments). Cells were identified by an
355 increase in resistance and often the presence of spikes in the test pulse. Loose seals (11-30 MΩ)
356 were made to cells using application of a small amount of negative pressure.

357 Sounds were presented to awake mice using a calibrated, free-field electrostatic
358 speaker (Tucker-Davis Technologies, ES1) positioned ~10 cm in front of the right ear
359 (contralateral to the IC recording site) at a ~45 ° angle relative to the midline of the mouse.
360 Sounds consisted of 1 s white noise bursts (4-64 kHz, 70 dB SPL) that were amplitude
361 modulated at 100% modulation depths using modulation frequencies ranging from 16 – 512 Hz
362 at 4 steps/octave. Each stimulus was repeated 8 times in a pseudorandomized order. After
363 collection of the control data, DQP or vehicle solution was infused into the brain at a rate of 0.1
364 µL/min while the sound presentation was repeated. Mice were recorded from no more than
365 once per day and for fewer than 7 sessions. After recording sessions were finished, the location
366 of the recordings was verified post hoc by dissection.
367

368 **Model neuron**

369 The model neuron used here was based, with minimal changes, on the fast-spiking
370 interneuron model described previously by Wang and Buzsáki (Wang and Buzsáki, 1996).
371 Simulated currents interacted with passive membrane properties according to the equation
372 $C_m \frac{dV}{dt} = -I_{Na} - I_K - I_L - I_{syn}$ where C_m = 1 µF/cm^2. Leak current was varied in the model to
373 approximate a range of membrane resistances that might be found in the IC, and the leak
374 reversal potential, E_L, was set to -65 mV.

375 Action potentials were modeled using Hodgkin-Huxley-type, voltage-dependent Na^+ and
376 K^+ conductances (Hodgkin and Huxley, 1952). The transient sodium current is described as
377 $I_{Na} = g_{Na} m^3{}_\infty h(V - E_{Na})$ where the activation variable *m* is assumed to be fast, and is thus
378 substituted by its steady state function $m_\infty = \frac{\alpha_m}{\alpha_m + \beta_m}$ where $\alpha_m(V) = -0.1 \frac{V + 35}{e^{-0.1(V+35)} - 1}$ and
379 $\beta_m(V) = 4e^{-\frac{V+60}{18}}$. The inactivation variable *h* obeys first order kinetics, where $\frac{dh}{dt} =$
380 $\varphi(\alpha_h(1 - h) - \beta_h h)$, $\alpha_h(V) = 0.07e^{-\frac{V+58}{20}}$, and $\beta_h(V) = \frac{1}{e^{-0.1(v+28)} + 1}$. The sodium conductance
381 was set to g_{Na} = 35 mS/cm^2 with a reversal potential E_{Na} = 55 mV.

382 The delayed rectifier potassium channel was modeled as $I_K = g_K n^4 (V - E_K)$, where
383 the activation variable *n* is given by $\frac{dn}{dt} = \varphi(\alpha_n(1 - n) - \beta_n n$. Here, $\alpha_n(V) = -0.01 \frac{V+34}{e^{-0.1(V+34)} - 1}$

384 and $\beta_n(V) = 0.125e^{-\frac{V+44}{80}}$, and we set the potassium conductance to g_K = 9 mS/cm^2 with a
385 reversal potential E_K = -90 mV.
386 Simulations using the model neuron were performed in MATLAB Version 2022a-2024a
387 (MathWorks) using custom MATLAB scripts adapted from functions provided in (Börgers,
388 Christoph, 2017). All code used for the model simulations can be found at:
389 https://github.com/audreydrotos/NMDA_modeling .
390
391 **Statistical analyses**
392 Data analysis was performed using custom algorithms and statistical packages in Igor
393 Pro 8, MATLAB R2021a-2024a (MathWorks), and R 4.1.0 (The R Project for Statistical
394 Computing). Statistical hypothesis testing was performed using two approaches. Comparisons
395 between control and drug condition data for in vitro experiments were made using linear mixed
396 model (LMM) analyses, which were conducted in R using the "lme4" and "lmerTest" packages
397 (Bates et al., 2015; Kuznetsova et al., 2017). Note that in cases where two groups were being
398 compared, the *p*-values from the LMM are identical to those obtained from a paired-samples *t*-
399 test (Shravan Vasishth et al., 2022). For comparisons between control and vehicle or drug
400 conditions in vivo, we used a Wilcoxon Signed Rank test, which was performed using the
401 'signrank' function in MATLAB. Effects were considered significant when $p < 0.05$.
402 For in vitro electrophysiology data involving repeated measures from individual cells,
403 effect sizes and confidence intervals are shown using Gardner-Altman estimation plots (two
404 groups) or Cumming estimation plots (three groups). These plots were made using custom
405 MATLAB scripts modeled after the DABEST package (Ho et al., 2019). Both types of estimation
406 plots use parallel coordinate plots to show the responses of individual cells for each condition,
407 and these are accompanied by histograms showing the range and 95% confidence intervals of
408 the paired mean differences expected between each drug condition and the control based on a
409 bootstrap analysis. Our approach to generating these plots has been detailed previously
410 (Rivera-Perez et al., 2021) and was influenced by the estimation statistics approach (Bernard,
411 2019; Calin-Jageman and Cumming, 2019). While estimation plots are provided to give

412 additional insight into the data, all determinations of statistical significance were based on the
413 standard null-hypothesis statistical tests detailed in the preceding paragraph.
414
415 **Results**
416 **NMDAR currents in VIP neurons are sensitive to GluN2C/D-specific pharmacology**
417 Several previous studies have noted that NMDARs often contribute to subthreshold
418 postsynaptic responses in IC neurons (Kelly and Zhang, 2002; Ma et al., 2002; Wu, 2004; Oberle
419 et al., 2022) . Similarly, we recently found that NMDARs contributed to subthreshold EPSPs
420 elicited by commissural inputs to IC VIP neurons (Goyer et al., 2019). NMDAR currents at resting
421 potential are unusual, as most NMDARs in the adult brain have a voltage-dependent Mg^{2+} block
422 which prevents ions from flowing through the channel pore at or near resting potential
423 (Traynelis et al., 2010; Paoletti et al., 2013). However, sensitivity to Mg^{2+} block depends on the
424 subunit composition of the receptor. While receptors containing GluN2A/B subunits are highly
425 sensitive to Mg^{2+} block, receptors containing GluN2C/D subunits are less sensitive, allowing
426 them to conduct current even at hyperpolarized potentials (Siegler Retchless et al., 2012).
427 Based on this, we hypothesized that VIP neurons express NMDARs containing GluN2C and/or
428 GluN2D subunits.
429 To test this hypothesis, we voltage-clamped VIP neurons at -70 mV and used a puffer
430 pipette containing 1 mM glutamate to elicit EPSCs (**Figure 1A**). We found that 10 ms glutamate
431 puffs reliably elicited EPSCs in VIP neurons (**Figure 1B**). We next performed puffs in the
432 presence of 1.5 µM PPDA, a GluN2C/D-selective antagonist (Lozovaya et al., 2004; Li et al.,
433 2020; Jing et al., 2022), and then in the presence of 20 µM CIQ, a GluN2C/D-selective positive
434 allosteric modulator (Mullasseril et al., 2010; Feng et al., 2014; Zhang et al., 2014; Nouhi et al.,
435 2018; Liu et al., 2021). PPDA significantly decreased the amplitude (LMM: $p = 0.038$) of the
436 elicited EPSC. Our experimental design did not favor large CIQ effects since we used a
437 saturating glutamate concentration (1 mM) in our puff solution. At the population level, CIQ did
438 not alter the amplitude ($p = 0.088$), halfwidth ($p = 0.15$), rise time ($p = 0.49$), or decay tau ($p =$
439 0.10) of the EPSC (**Figure 1C**). The sensitivity of NMDAR currents in VIP neurons to PPDA and, in

440 some cases to CIQ, suggests that at least a portion of the NMDARs expressed in VIP neurons
441 contain GluN2C/D subunits.
442
443 **Many IC neurons in adult mice express *Glun2c* and/or *Glun2d* mRNA, with VIP neurons**
444 **predominately expressing *Glun2d***
445 GluN2C and GluN2D subunits are similar in their sensitivity to Mg^{2+} block, but expression
446 levels of *Glun2c* and *Glun2d* mRNA change dramatically and in different directions during
447 development (Paoletti et al., 2013). GluN2D-containing NMDARs (along with GluN2B-containing
448 NMDARs) are primarily found early in development (Wenzel et al., 1996) and are largely
449 replaced with GluN2A and GluN2C subunits by adulthood (Paoletti et al., 2013), with some
450 exceptions in small populations of interneurons, such as those found in hippocampus (Monyer
451 et al., 1992). In many cases, the developmental switch in NMDAR subunit composition is
452 thought to be driven by sensory experience (Traynelis et al., 2010). Expression of GluN2
453 subunits is also spatially regulated: while GluN2A and GluN2B-containing NMDARs are typically
454 found at the synapse, GluN2C and GluN2D-containing NMDARs are often found at extrasynaptic
455 sites (Paoletti et al., 2013). However, growing evidence points to GluN2C/D expression at
456 synapses, such as in striatum (Logan et al., 2007) and substantia nigra (Brothwell et al., 2008).
457 Based on these precedents, we hypothesized that IC VIP neurons in adult animals
458 express GluN2C subunits. To test this hypothesis, we used the RNAScope assay to perform
459 fluorescence in situ hybridization on IC brain slices from three VIP-IRES-Cre x Ai14 mice aged
460 P45-47 (**Figure 2A,B**). Using probes for *tdTomato*, *Glun2c*, and *Glun2d* mRNA, we were
461 surprised to find that 91.4% of VIP neurons expressed *Glun2d* and only 8.1% expressed *Glun2c*.
462 More specifically, 84.3% of VIP neurons expressed only *Glun2d*, 1.0% of VIP neurons expressed
463 only *Glun2c*, and 7.1% of VIP neurons expressed both. The remaining 7.7% of VIP neurons did
464 not express *Glun2c* or *Glun2d* (**Table 1**, **Figure 3A**).
465 We also investigated whether NMDAR subunit expression differed among VIP neurons
466 present in the three major IC subdivisions: central nucleus, dorsal cortex, and lateral cortex. We
467 found that the percentage of VIP neurons expressing various NMDAR subunits was similar
468 across all IC subdivisions (**Table 2**, **Figure 3B**). These results suggest that VIP neurons

469 preferentially express GluN2D rather than GluN2C subunits, regardless of their location in the
470 IC.
471 Importantly, our results also show that *Glun2c* and *Glun2d* mRNA is widely expressed in
472 the IC (**Figure 2A**). This suggests that *Glun2c* and *Glun2d*-containing NMDARs are a prominent
473 feature in the IC and likely have a significant and widespread impact on synaptic computations.
474
475 **VIP neurons also express GluN2A/B-containing NMDARs**
476 We next investigated whether IC VIP neurons also express GluN2A or GluN2B-containing
477 receptors. In the adult brain, GluN2A-containing NMDARs are more commonly found at
478 synapses and confer more typical properties of the NMDA receptor, including sensitivity to
479 Mg^{2+} block at rest (Siegler Retchless et al., 2012). To determine whether VIP neurons express
480 GluN2A/B-containing NMDARs in addition to GluN2C/D-containing NMDARs, we targeted VIP
481 neurons for whole-cell recordings and puffed glutamate in the presence of AMPAR antagonist
482 NBQX (10 µM, **Figure 4A**). To examine the contributions of all NMDARs to the resulting current,
483 we removed Mg^{2+} from the ACSF and replaced it with equimolar Ca^{2+} to maintain the overall
484 concentration of divalent ions. We found that puffs of glutamate elicited much larger currents
485 in the Mg^{2+}-free condition than we observed in the earlier puff experiments (compare **Figures**
486 **1C, 4C**).
487 Next, we bath applied 1.5 µM PPDA, a GluN2C/D-specific antagonist, and as expected,
488 we found that this significantly decreased the amplitude (LMM: p = 9.26e-4), halfwidth (p =
489 8.6e-4), rise time (p = 8.45e-3), and decay time constant (p = 0.028) of the response, again
490 suggesting that a portion of the NMDAR current in VIP neurons is mediated by GluN2C/D-
491 containing NMDARs (**Figure 4C**). Next, we bath applied 100 µM D-AP5, an NMDAR antagonist
492 that blocks NMDARs regardless of GluN2 subunit identity and found that this completely
493 abolished the response in all neurons (amplitude, p = 1.71e-4). Overall, 5 out of 6 VIP neurons
494 had both PPDA sensitive and Insensitive currents, indicating activation of both GluN2A/B and
495 GluN2C/D currents. On average in these cells, 82.0% ± 26.2% of the current was sensitive to
496 PPDA (mean ± standard deviation, **Figure 4D**). Two neurons had current that was completely
497 abolished by PPDA indicating exclusive activation of GluN2C/D-containing receptors. These

498 results suggest that individual VIP neurons can express NMDARs that differ by subunit
499 composition and are thus specialized for different roles in the cell.
500
501 **Commissural inputs to VIP neurons activate GluN2C/D-containing NMDARs**
502 We previously found that inputs from the contralateral IC via the IC commissure activate
503 NMDARs on VIP neurons at resting potential (Goyer et al., 2019). To test whether these
504 responses were also mediated by GluN2C/D-containing NMDAR receptors, we repeated these
505 experiments in the presence of GluN2C/D-specific drugs. Commissural projections were labeled
506 with the excitatory opsin Chronos by injecting AAV-Synapsin-Chronos-GFP (serotype 1, 5, or 9)
507 into the right IC of VIP-IRES-Cre x Ai14 mice. 1.5 to 4 weeks later, we targeted whole-cell
508 recordings to fluorescently labeled VIP neurons in the IC contralateral to the injection site
509 (**Figure 5A**). We found that even in the presence of AMPAR antagonist NBQX (10 µM), flashes of
510 blue light elicited small EPSCs (-2 to -18 pA, **Figure 5B**). The GluN2C/D-specific positive allosteric
511 modulator CIQ did not alter the light-evoked response, again possibly because a saturating
512 concentration of glutamate was used and/or because CIQ is less effective at tri-heteromeric
513 NMDARs that contain a GluN2A/B subunit in addition to a GluN2C/D subunit (Mullasseril et al.,
514 2010) (**Figure 5C,** LMM: amplitude p = 0.86, halfwidth p = 0.064, rise time p = 0.26, decay tau
515 p = 0.17), but the GluN2C/D-specific antagonist PPDA completely abolished the response in all
516 cells tested (amplitude, LMM: p = 5.13e-3). These results support the hypothesis that
517 commissural inputs to VIP neurons activate NMDARs containing GluN2C/D subunits.
518
519 **Activation of GluN2C/D-containing NMDARs facilitates temporal summation**
520 Since NMDARs with GluN2C/D subunits have slower kinetics and conduct more current
521 at resting membrane potential than NMDARs with GluN2A/B subunits (Paoletti et al., 2013),
522 expression of GluN2C/D-containing NMDARs could have a particularly strong effect on the
523 duration of excitation elicited by glutamatergic transmission. We therefore hypothesized that
524 GluN2C/D-containing NMDARs in the IC facilitate temporal integration by widening the time
525 window for integration of synaptic inputs. To test this hypothesis, we used optogenetics to
526 stimulate commissural inputs to VIP neurons (**Figure 6A**). Trains of five light pulses at 30 Hz

527 elicited temporal summation in all the cells tested, with the second through fifth EPSPs starting
528 at a more depolarized potential than the first EPSP (**Figure 6B**). To test whether GluN2C/D-
529 containing receptors facilitate this temporal summation, we next elicited trains of input in the
530 presence of the GluN2C/D-containing NMDAR antagonist PPDA (1.5 µM). In one cell, the light
531 train elicited temporal summation great enough to elicit an action potential in the control
532 condition, and this was impaired in the PPDA condition, where the cell only reached action
533 potential threshold in one trial (**Figure 6C,D**). In trials that did not reach action potential
534 threshold, we assessed temporal summation by comparing the peak amplitudes of each of the
535 five EPSPs elicited by the train stimuli in the control and PPDA conditions (**Figure 6B**). The
536 amplitude of the peaks significantly increased during the train (LMM: p = 9.15e-6, n = 5, **Figure**
537 **6E**) indicating temporal summation occurred during the train. This change in amplitude was not
538 correlated with small changes in the resting membrane potential over the course of the
539 recording (r^2 = 0.001). In addition, PPDA significantly decreased the area under the curve of the
540 train response (LMM: p = 0.038, **Figure 6F**), indicating a decrease in temporal summation when
541 GluN2C/D-containing receptors were blocked. These results show that GluN2C/D-containing
542 NMDARs strongly enhance the time window for synaptic integration in VIP neurons.
543

544 **GluN2C/D-containing NMDA receptors provide additive gain to rate coding in a neuron model**

545 Our in vitro data suggest that GluN2C/D-containing receptors facilitate synaptic
546 integration in IC neurons, and we hypothesized that this boosts gain in the IC through an
547 increase in temporal summation, which could in turn promote rate coding for auditory stimuli.
548 To test this hypothesis, we created a neuron model based on a previously published Hodgkin-
549 Huxley model of fast-spiking hippocampal interneurons (Wang and Buzsáki, 1996). We based
550 our model on the Wang and Buzsáki model because it provides a well-known and widely used
551 model for neurons that exhibit sustained firing over a large range of synaptic input frequencies,
552 similar to what we observe for VIP neurons in vitro (Goyer et al., 2019). In our adapted model,
553 we included two synaptic conductances: one with kinetics similar to AMPA receptors on VIP
554 neurons, and one with kinetics similar to a GluN1-GluN2D-GluN2D NMDA receptor (Yi et al.,
555 2019). We set the maximal NMDA conductance to 25% of the maximal AMPA conductance and

556 set the leak conductance to 0.7 mS/cm^2 to mimic the average membrane resistance of a VIP
557 neuron (~200 MΩ), assuming a 15 µm diameter soma (Goyer et al., 2019). We next simulated
558 trains of synaptic inputs at frequencies ranging from 16 – 512 Hz, activating either the AMPA
559 conductance alone or both the AMPA and NMDA conductances.

560 We found that activation of the AMPA-only synapse by a slow train of stimuli (16 Hz)
561 elicited a series of phase-locked EPSPs in the model neuron (**Figure 7A**, left panel). When the
562 NMDA conductance was added, the slow kinetics of the NMDA receptor caused the EPSPs to
563 temporally sum across stimulus presentations, providing an additive gain that pushed the
564 neuron over action potential threshold and elicited phase-locked action potentials (**Figure 7A**,
565 right panel). When the input frequency was increased to 64 Hz, the neuron fired phase-locked
566 action potentials in the AMPA-only condition (**Figure 7B**, left panel), and addition of the NMDA
567 conductance again increased the overall firing rate (**Figure 7B**, right panel). To better examine
568 how the NMDA conductance shapes the response to inputs at different stimulus frequencies,
569 we simulated the response using input frequencies from 16 – 512 Hz (4 steps/octave) in both
570 the AMPA-only and AMPA plus NMDA conditions. We found that addition of the NMDA
571 conductance caused an overall increase in firing rate in response to all input frequencies tested
572 (**Figure 7C**, orange line). Addition of the NMDA conductance also altered phase-locking to the
573 response (**Figure 7D**): in the AMPA-only condition, the neuron exhibited near perfect phase
574 locking as soon as the input frequency was high enough to elicit spiking (blue line). When the
575 NMDA conductance was added (orange line), phase locking was high at lower input frequencies
576 but quickly became poorer as the input frequency increased, an effect due in part to the slow
577 kinetics of the NMDA receptor which decreased the ability of the fast, temporally precise AMPA
578 conductance to facilitate phase-locking in the model neuron. In line with this, addition of the
579 NMDA conductance shifted the phase of the input response at which the neuron fired (**Figure**
580 **7E**). These results suggest that GluN2C/D-type NMDA receptors provide additive gain to neuron
581 input-output functions, in the form of an upward shift along the *y*-axis of firing vs stimulus
582 curves (e.g., **Figure 7C**) (Silver, 2010). Our model also indicates that, as stimulus frequencies
583 increase, this type of additive gain increases firing rate while simultaneously decreasing the
584 precision of spike timing.

585

586 **Membrane resistance alters modulation of rate coding by GluN2C/D-containing NMDARs**

587 IC neurons are heterogeneous in their intrinsic physiology (reviewed in Drotos and
588 Roberts, 2024), and these differences may alter how AMPA and NMDA receptors contribute to
589 temporal and rate coding for stimuli. To examine how membrane resistance influences
590 temporal integration, we simulated rate and temporal modulation transfer functions (MTFs) to
591 input trains with frequencies between 16 – 512 Hz, as above, in model neurons where the leak
592 conductance (g_L) was set to 0.282, 0.50, 0.75, 1.99, and 5.3 mS/cm^2 (corresponding to
593 membrane resistances of 502, 283, 189, 71, and 27 MΩ, respectively, assuming 15 µm cell
594 diameter). At the three lowest values for g_L, neurons exhibited high-pass rate MTFs with a
595 relatively smooth increase in firing rate as input frequency increased (**Figure 8A-C**, left panel).
596 These cells also exhibited temporally precise firing at slow input frequencies, but the temporal
597 precision of firing fell apart at higher input frequencies, and overall, the firing rate provided a
598 more consistent indicator of input frequency. In addition, in these cells, the NMDA conductance
599 contributed additive gain to the rate MTFs that shifted the input-output functions upwards
600 along the *y*-axis, towards higher firing rates.

601 As the leak conductance increased to 1.99, and 5.3 mS/cm^2, we observed two major
602 shifts: first, neurons increasingly exhibited better phase-locking and poorer rate coding of the
603 input frequency, and second, addition of the NMDA conductance began to decrease, rather
604 than increase, the gain of the rate MTF (**Figure 8D,E**). In our model, this was due to the
605 additional conductance causing depolarization block, which shifted the response profile of
606 these cells to an onset response. Note that rate MTFs in **Figure 8D,E** decreased to one spike per
607 stimulus train, not zero, at higher input frequencies, and vector strengths were only calculated
608 when input trains elicited >4 spikes per train. While it is likely that adding low-voltage-activated
609 K^+ conductances and/or other voltage-gated conductances to the model could convert onset
610 firing neurons to phasic firing neurons, our main goal here was to mimic VIP neurons and other
611 IC neurons with sustained firing, where such conductances are not prominent (Goyer et al.,
612 2019). Overall, our modeling results highlight that the intrinsic physiology of a neuron

613 influences both how that neuron uses temporal and rate codes for stimuli and how NMDA
614 receptors shape these codes.
615
616 **GluN2C/D-containing receptors enhance gain for encoding AM stimuli**
617 The results from our optogenetics experiments and neuron model suggest that NMDA
618 receptors shape temporal and rate coding of synaptic stimuli. In the IC, temporal and rate codes
619 are particularly important for encoding amplitude-modulated (AM) sounds, as IC neurons can
620 encode the modulation frequency of AM stimuli with changes in firing rate and/or by phase-
621 locking their firing to the modulation waveform (Krishna and Semple, 2000). Based on our
622 model results, we hypothesized that GluN2C/D-containing NMDA receptors contribute to rate
623 coding in the IC by broadening the time window for integrating phase-locked synaptic inputs
624 and enhancing firing rates across different modulation frequencies. In support of this
625 hypothesis, Zhang and Kelly showed that blocking NMDARs decreased rate coding in IC neurons
626 while leaving temporal coding of AM stimuli intact (Zhang and Kelly, 2001), similar to what we
627 observed in our model neuron (**Figures 7,8**). To examine how GluN2C/D-containing NMDARs
628 influence rate coding for AM stimuli in the mouse IC, we made juxtacellular (loose-patch)
629 current-clamp recordings from IC neurons in awake, headfixed mice while playing 1 s
630 broadband noise bursts (4-64 kHz) that were amplitude modulated with modulation
631 frequencies of 16 – 512 Hz and 100% modulation depths (**Figure 9A**).
632 In line with previous studies, we found that IC neurons encode AM stimuli via changes in
633 firing rate (rate coding) and by phase locking their firing to the modulation waveform (temporal
634 coding) (example cell response, **Figure 9B**). We next found that local infusion of 20 µM DQP, a
635 GluN2C/D-selective antagonist, significantly decreased the firing rate during AM stimuli (signed-
636 rank test, p = 0.042, median difference = -1.11 Hz) (**Figure 9C,F**) but had no effect on the
637 average phase-locked responses (vector strength, signed-rank test, p = 0.19, median difference
638 = -0.008) (**Figure 9C,G**) or the phase of the modulation frequency at which the neuron fired
639 (**Figure 9E**). Overall, blocking GluN2C/D-containing receptors did not alter the shape of rate or
640 temporal modulation transfer functions, nor did it significantly alter the relative change in firing
641 rates (max – min) across the range of AM stimuli (dynamic range, p = 0.067, median difference

642 = -0.13 Hz, **Figure 9H**). However, blocking GluN2C/D-containing receptors did significantly
643 decrease the spontaneous firing rate during periods between stimulus presentations (p = 0.024,
644 median difference = -3.03 Hz, **Figure 9I**). Together, these results suggest that GluN2C/D-
645 containing receptors influence rate coding in IC neurons by providing a tonic, additive boost in
646 gain to both spontaneous and sound-evoked synaptic inputs.
647 In addition, we ran control experiments to evaluate whether changes in firing could be
648 due to infusion of solution into the IC or drift in the firing rate over the course of each
649 recording. We found that infusion of vehicle solution did not alter the firing rate during AM
650 stimuli (p = 0.74, median difference = -0.062 Hz), the vector strength of the response (p = 0.063,
651 median difference = -0.018), the dynamic range in response to AM stimuli (p = 0.086, median
652 difference = -0.12 Hz), or the spontaneous firing rate between sound presentations (p = 0.20,
653 median difference = 0.76 Hz) (vehicle panels, **Figure 9D-I**).
654
655 **Discussion**
656 In this study, we found that GluN2C/D-containing NMDARs shape synaptic integration
657 and auditory processing in the IC. By combining optogenetics with whole-cell recordings, we
658 found that NMDARs in VIP neurons are activated at resting potential by commissural
659 projections. By using puffs of glutamate and whole-cell recordings combined with GluN2C/D-
660 specific pharmacology, we showed that GluN2C/D-containing NMDARs activate at resting
661 potential in VIP neurons. We demonstrated that 91% of VIP neurons express mRNA for the
662 GluN2D subunit. We also found that *Glun2c* and *Glun2d* mRNA is prevalent throughout the IC,
663 including in many non-VIP neurons, suggesting that GluN2C/D-containing NMDARs exert
664 widespread influence over excitatory postsynaptic responses in the IC. Additionally, we
665 demonstrated that VIP neurons can also express GluN2A/B-containing receptors, suggesting
666 that different types of NMDARs may play distinct roles in these cells. Finally, we showed that
667 GluN2C/D-containing receptors facilitate temporal summation in VIP neurons in vitro, provide
668 additive gain to neuron input-output functions in silico, and enhance the spontaneous and
669 sound-evoked firing rates of IC neurons in vivo. Thus, NMDAR diversity shapes synaptic
670 integration and thus auditory processing in the IC.

671

672 **VIP neurons express NMDARs with GluN2D subunits**

673 One of the most intriguing findings from our study was that the NMDAR currents
674 elicited at resting potential in VIP neurons were predominately attributable to GluN2D-
675 containing NMDARs rather than GluN2C. This result was unexpected for two reasons: first, in
676 most brain regions, expression of *Glun2d* mRNA is developmentally regulated and disappears in
677 adulthood (Monyer et al., 1994; Wenzel et al., 1996). Second, in adult animals, GluN2D-
678 containing NMDARs are conventionally thought to be restricted to extrasynaptic locations, for
679 example, in dorsal horn neurons (Momiyama, 2000) and Golgi cells of the cerebellum (Misra et
680 al., 2000; Brickley et al., 2003), but there are some exceptions, such as in spinal cord laminar
681 cells (Hildebrand et al., 2014). In addition, NMDARs are highly motile and can rapidly diffuse
682 between extrasynaptic and synaptic sites (Tovar and Westbrook, 2002), as occurs during
683 learning. During induction of NMDAR-LTP in the medial perforant path of the dentate gyrus,
684 GluN2D-containing NMDARs are trafficked to the synapse where they contribute to synaptic
685 transmission (Harney et al., 2008). Based on this, we hypothesize that GluN2D-containing
686 receptors diffuse to synaptic locations on VIP neurons during learning. An alternative
687 hypothesis is that GluN2D-containing NMDARs are natively found in the synapse and do not
688 undergo a GluN2D-to-GluN2A/C switch during development.

689 Additionally, while we show here that many NMDARs on VIP neurons contain the
690 GluN2D subunit, the full subunit composition of the receptor remains unknown. NMDARs are
691 tetrameric receptors made up of four subunits, including two obligatory GluN1 subunits and a
692 combination of GluN2A-D and/or GluN3 subunits (Traynelis et al., 2010). Our in situ
693 hybridization results showed that 91% of VIP neurons express *Glun2d* mRNA. This could give
694 rise to NMDARs that are diheteromeric with two GluN1 subunits and two GluN2D subunits.
695 However, GluN1-GluN2D receptor assemblies have much slower kinetics than we observed in
696 our study (decay τ = 10-100 ms), with decay time constants on the order of 2 seconds (Vicini et
697 al., 1998). An alternative hypothesis is that GluN2D-containing receptors in VIP neurons are
698 triheteromeric GluN1-GluN2B-GluN2D complexes. These receptors display properties that are
699 intermediate to those of GluN1-GluN2B and GluN1-GluN2D receptors, including slightly faster

700 kinetics than GluN1-GluN2D assemblies (Yi et al., 2019) and a reduced sensitivity to Mg^{2+} block
701 compared to GluN1-GluN2B assemblies (Huang and Gibb, 2014). In addition, receptors
702 containing GluN2B tend to be more motile than NMDARs with GluN2A subunits (Groc et al.,
703 2006). Thus, this proposed GluN1-GluN2B-GluN2D assembly may also help explain how
704 GluN2D-containing receptors contribute to synaptic transmission in mature VIP neurons. This
705 conclusion is also supported by our CIQ experiments: we found a small effect of CIQ in the puff
706 experiments and no effect of CIQ in the optogenetic activation experiments. The ability of CIQ
707 to potentiate GluN2C/D-containing receptors is diminished in triheteromeric receptor
708 assemblies compared to diheteromeric ones (Mullasseril et al., 2010), suggesting that the
709 receptors studied here may be triheteromeric.
710
711 **Distribution of NMDARs on VIP neurons is synapse-specific**
712 Previous work from our lab showed that NMDAR activation at resting potential on VIP
713 neurons occurs with commissural inputs but not inputs from the DCN (Goyer et al., 2019). This
714 suggests that the distribution of NMDARs on VIP neuron synapses is pathway-dependent, with
715 commissural inputs targeting synapses that are enriched in GluN2D-containing receptors while
716 DCN inputs target synapses predominated by AMPARs and possibly GluN2A/B-containing
717 NMDARs. Heterogeneity in NMDAR composition at IC neuron synapses is also supported by the
718 results from our in vitro and in vivo experiments, where some cells exhibited greater magnitude
719 changes in response to blockade of GluN2C/D-containing NMDARs as compared to other cells.
720 Such differences in receptor distribution could underlie functional differences between these
721 synapses, as has been seen in other brain regions such as neocortex (Kumar and Huguenard,
722 2003). For example, commissural inputs may be integrated over longer time scales than those
723 from the DCN, and a neuron may require more DCN inputs within a smaller time window to
724 generate a postsynaptic spike.
725 NMDAR subtype distribution might also affect synaptic plasticity. GluN2A/B-containing
726 NMDARs have been well-studied for their role in the initiation of long-term potentiation (LTP)
727 (Paoletti et al., 2013). In the IC, previous studies show that electrical stimulation of the lateral
728 lemniscus can induce LTP in IC neurons (Hosomi et al., 1995), and NMDARs are required for this

729 process (Zhang and Wu, 2000; Wu et al., 2002). Our glutamate puff experiments showed that
730 VIP neurons also express GluN2A/B-containing NMDARs, indicating that at least some VIP
731 neuron synapses may exhibit AMPAR-dependent LTP (Malenka and Nicoll, 1993; Rebola et al.,
732 2010; Hunt and Castillo, 2012). It will be important for future studies to determine the
733 contributions of GluN2D trafficking and GluN2A/B expression to synaptic plasticity in the IC.
734

735 **GluN2D-containing receptors may alter rate coding for stimuli in the IC**

736 Auditory structures primarily encode changes in sound amplitude envelopes in two
737 ways: using temporal codes, where neurons phase-lock their firing to the modulation
738 waveform, and using rate codes, where a neuron's firing rate changes based on the frequency
739 of the amplitude modulation (AM). While early auditory structures such as the cochlear nucleus
740 primarily use temporal codes for AM stimuli (Rhode and Greenberg, 1994), neurons in auditory
741 cortex primarily use rate codes (Yin et al., 2011). Since many IC neurons only phase lock to
742 lower AM modulation frequencies (Rees and Møller, 1983; Rees and Palmer, 1989; Krishna and
743 Semple, 2000) but exhibit strong and diverse dependencies of firing rate on changes in AM
744 modulation frequency (Krishna and Semple, 2000; Nelson and Carney, 2007; Geis and Borst,
745 2009; Kim et al., 2020), the IC has been proposed as a critical site for the temporal-to-rate code
746 transition that occurs between brainstem and cortex.

747 Our model and in vivo data highlight multiple important considerations for this
748 transition. First, our model VIP neuron (**Figure 7**) and in vivo data (**Figure 9**) show that NMDA
749 receptors contribute additive gain for rate coding of AM stimuli, providing a boost that pushes
750 the neuron closer to spike threshold and increases the overall firing rate across modulation
751 frequencies. This provides evidence for a mechanism that may promote rate coding in IC
752 neurons by enhancing the dynamic range over which neurons encode AM modulation
753 frequency using changes in firing rate. Second, when we investigated how adding an NMDA
754 conductance altered temporal and rate coding in our model neuron, we found that the coding
755 shifts were highly dependent on the input resistance of the neuron. Cells modeled with a lower
756 leak conductance (**Figure8A-C**) and thus higher input resistance had clear rate coding for AM
757 stimuli but exhibited poorer phase-locking. Addition of the NMDA conductance to the higher

758 input resistance models provided additive gain which increased firing output, similar to what
759 was seen in our in vivo experiments (**Figure 9C,F**). However, neurons modeled with a higher
760 leak conductance and thus lower input resistance tended to exhibit stronger phase locking and
761 poorer rate coding. In addition, adding the NMDA conductance to these models pushed the cell
762 into depolarization block at higher input frequencies, thus turning the model neuron into a cell
763 with an onset response profile.
764 Overall, our results show that GluN2C/D-containing NMDA receptors interact with
765 AMPA receptors and passive membrane properties to shape rate and temporal coding in many
766 IC neurons, helping give rise to the diverse ways that IC neurons encode AM stimuli and other
767 temporally modulated sounds.
768
769

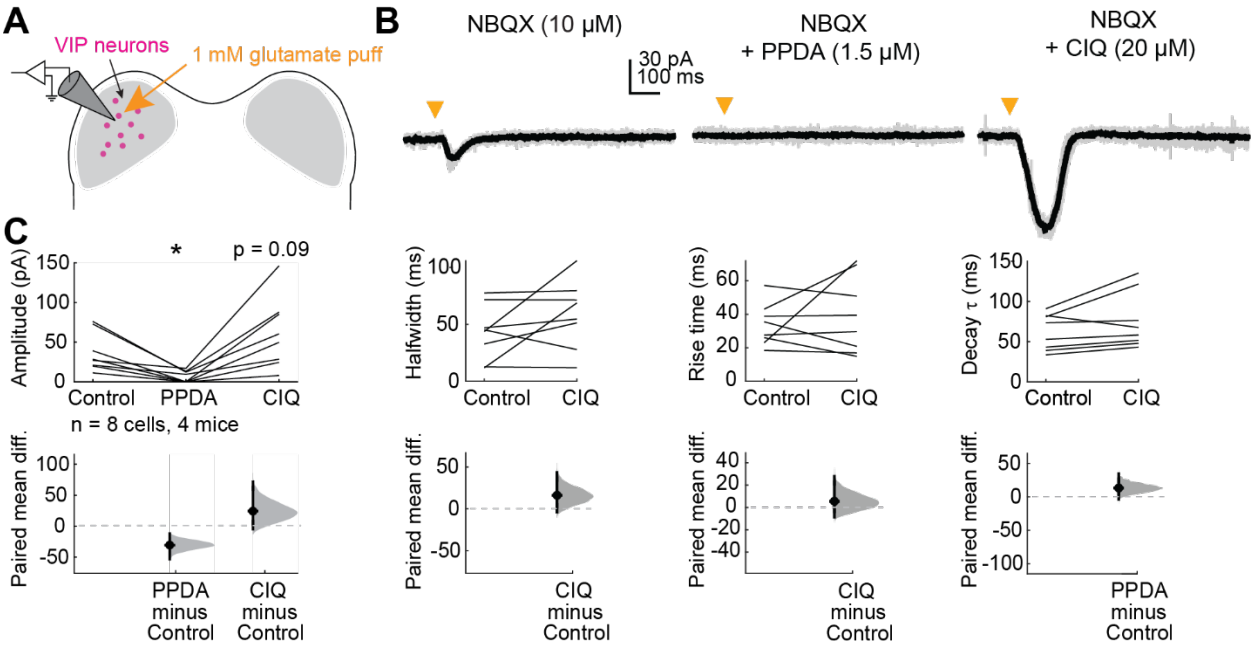

Figure 1. VIP neurons express GluN2C/D-containing NMDARs

A, Puffs of glutamate onto VIP neurons activated NMDARs. Pharmacology was used to examine whether GluN2C/D-containing receptors contributed to elicited currents. ***B,*** Brief (10 ms) puffs of glutamate onto a VIP neuron elicited a small inward current (left) which was completely abolished by the GluN2C/D antagonist PPDA (middle) and enhanced by the GluN2C/D positive allosteric modulator CIQ (right). ***C,*** PPDA decreased the amplitude (LMM: β = -30.46, 95% CI [-56.32, -4.61], p = 0.038, n = 8) of the response to the glutamate puff. CIQ trended towards enhancing the amplitude (β = 24.33, 95% CI [-1.53, 50.18], p = 0.088, n = 8) of the response, but did not alter the halfwidth (β = 16.13, 95% CI [-7.89, 37.16], p = 0.15, n = 8), rise time (β = 5.56, 95% CI [-10.24, 21.36], p = 0.49, n = 8) or decay τ (β = 13.23, 95% CI [-1.29, 27.74], p = 0.10, n = 8) of the response to the glutamate puff. Vertical black lines on the paired mean difference plots indicate 95% bootstrap confidence intervals, and gray histograms show the expected distribution of paired mean differences based on bootstrap analysis.

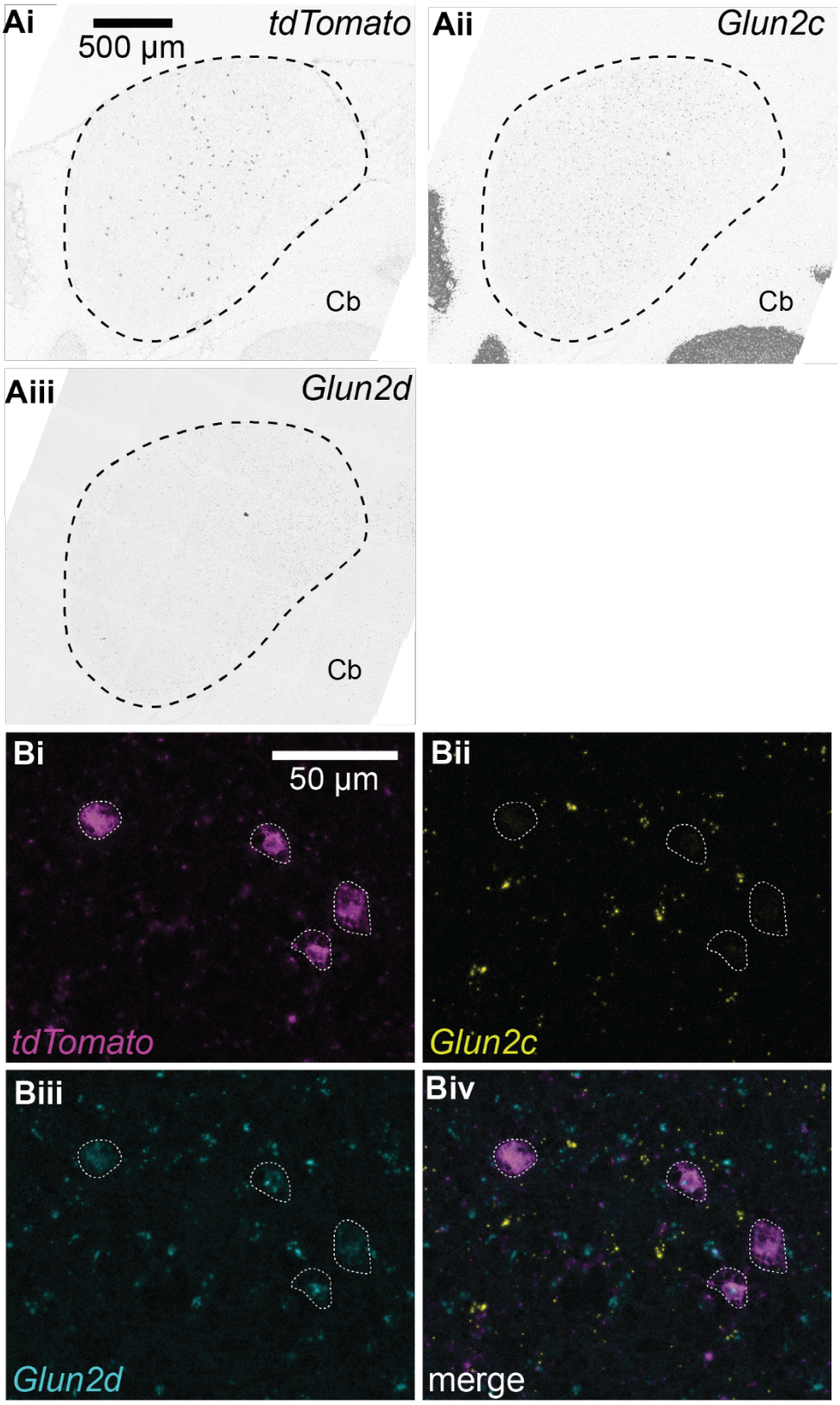
Ai
500 µm
tdTomato
Cb
Aii
Glun2c
Cb
Aiii
Glun2d
Cb
Bi
50 µm
tdTomato
Bii
Glun2c
Biii
Glun2d
Biv
merge

785

786 **Figure 2. *Glun2c and Glun2d* mRNA is widely expressed throughout the IC, and most VIP**
787 **neurons express *Glun2d***
788 ***A,*** 40x confocal images of IC brain slices following RNAscope in situ hybridization showing
789 expression of *tdTomato* mRNA ***(i),*** which is expressed by VIP neurons in VIP-IRES-Cre x Ai14
790 mice, *Glun2c* mRNA ***(ii)***, and *Glun2d* mRNA ***(iii)***. 'Cb' indicates portions of the cerebellum that
791 were captured in the images. ***B,*** 63x confocal images with white arrows indicating *tdTomato*-
792 positive neurons ***(i)***. 8.1% of *tdTomato* positive neurons expressed *Glun2c* mRNA ***(ii)*** and 91.4%
793 expressed *Glun2d* mRNA ***(iii)***. *Glun2c* and *Glun2d* mRNA was also commonly observed in
794 tdTomato-negative neurons, suggesting that these NMDAR subunits are expressed in multiple
795 IC neuron types. A merge of these images is shown in ***iv***.
796

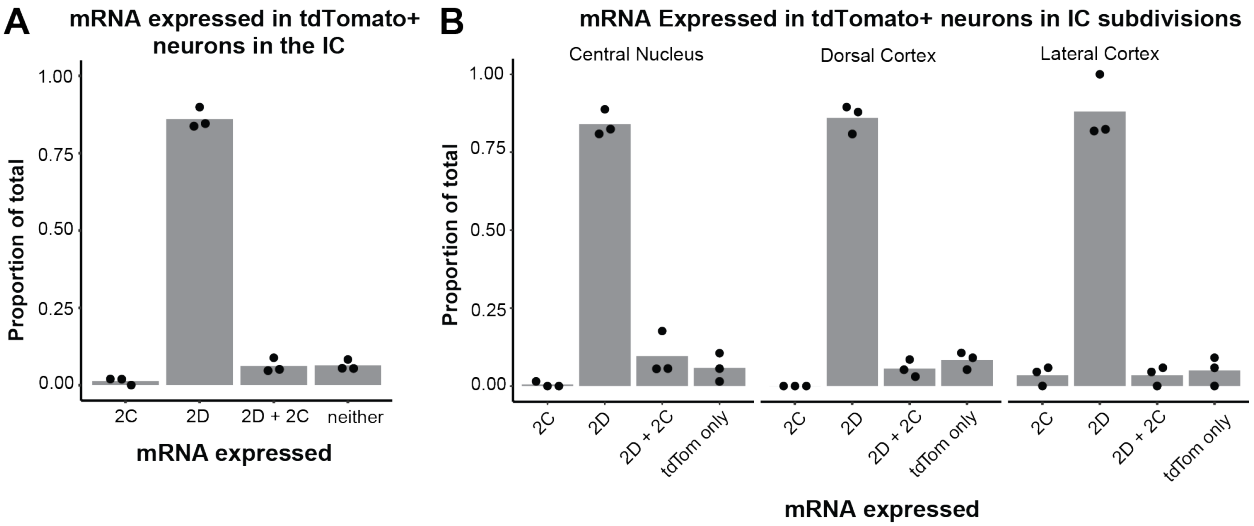

Figure 3. 91.4% of VIP neurons express *Glun2d* mRNA

A, Quantification of mRNA expressed in *tdTomato*-positive (VIP) neurons in the IC. 1.0% of VIP neurons expressed only *Glun2c* mRNA, while 84.3% of VIP neurons expressed only *Glun2d* mRNA. 7.1% of VIP neurons expressed both *Glun2c* and *Glun2d* mRNA. 7.7% of VIP neurons did not express *Glun2c* or *Glun2d* mRNA. Individual data points represent the mean for individual mice. ***B,*** The central nucleus, lateral cortex, and dorsal cortex of the IC did not differ in their expression profiles of tdTomato-positive neurons expressing only *Glun2c* (0.8%, 0.0%, 3.8%, respectively), only *Glun2d* (83.7%, 85.0%, 86.5%), both *Glun2c* and *Glun2d* (7.9%, 6.2%, 3.8%), and neither *Glun2c*/*Glun2d* (7.6%, 8.8%, 5.8%). Individual data points represent the means for individual mice.

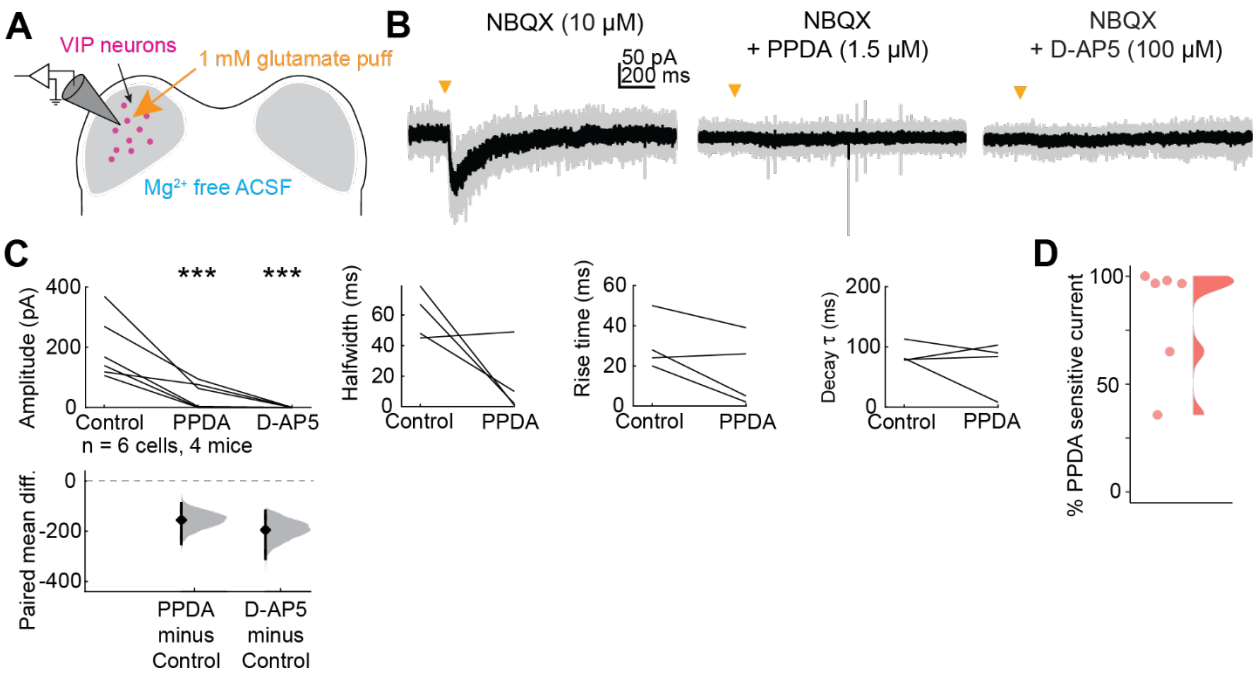

Figure 4. VIP neurons express GluN2A/B-containing NMDARs in addition to GluN2C/D-containing NMDARs

A, Puffs of glutamate onto VIP neurons activated NMDARs. Pharmacology was used to examine the proportion of GluN2A/B and GluN2C/D containing receptors present on VIP neurons. ***B,*** An EPSC elicited by a brief (10 ms) puff of glutamate onto a VIP neuron was abolished by application of the GluN2C/D antagonist PPDA. ***C,*** PPDA decreased the amplitude (β = -155.49, 95% CI [-220.62, -90.36], *p* = 9.26e-4, *n* = 6) of the response to the glutamate puff. D-AP5 completely abolished the response in all cells tested (amplitude, LMM: β = -194.83, 95% CI [-259.96, -129.70], *p* = 1.71e-4, *n* = 6). Effects on EPSC kinetics for cells with residual current after PPDA application are shown in ***C,*** right panels. Vertical lines on the paired mean difference plots indicate 95% bootstrap confidence intervals, and gray histograms show the expected distribution of paired mean differences based on bootstrap analysis. ***D,*** Percent of EPSC amplitude that was sensitive to PPDA application in each of the 6 cells from **C**. The distribution was created using the 'ggdist' and 'stat_halfeye' functions from the 'ggplot' package for R, which uses a kernel density estimate to generate a curve that reflects the distribution of the data (Kay, 2024).

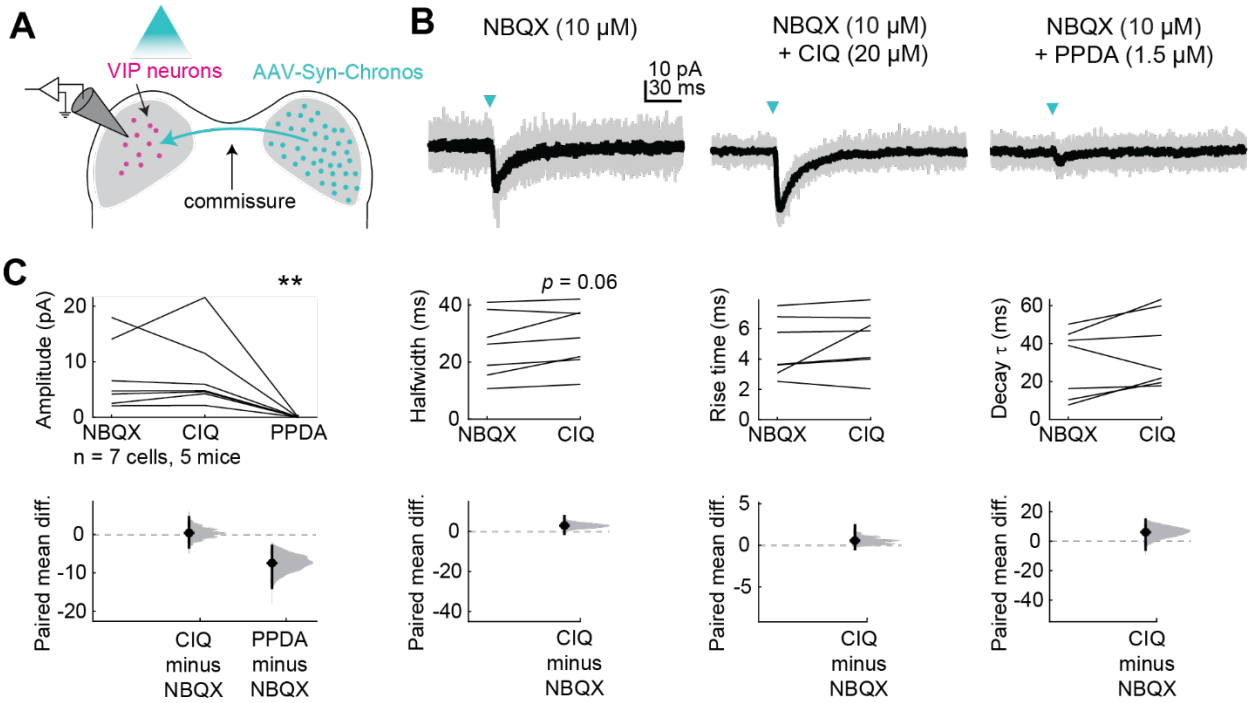

Figure 5. Commissural inputs to VIP neurons activate GluN2C/D-containing NMDARs at resting potential.

A, Viral injections in the right IC drove Chronos expression in commissural projections to the left IC. Optogenetic circuit mapping and pharmacology were used to examine postsynaptic responses in VIP neurons in the left IC. ***B,*** An EPSC elicited by a brief (10 ms) flash of light (left) was enhanced by the GluN2C/D-specific positive allosteric modulator CIQ (middle) and diminished by the GluN2C/D-specific antagonist PPDA (right). ***C,*** CIQ did not significantly alter the amplitude (LMM: β = 0.39, 95% CI [4.63, -3.86], p = 0.86, n = 7), halfwidth (β = 2.95, 95% CI [0.22, 5.69, p = 0.064], p = 0.42, n = 7), rise time (β = 0.56, 95% CI [-0.38, 1.50], p = 0.26, n = 7), or decay τ (β = 6.13, 95% CI [-2.02, 14.27], p = 0.16, n = 7) of EPSCs. PPDA abolished the response in all cells tested (amplitude, LMM: β = -7.44, 95% CI [-11.68, -3.20], p = 5.13e-3, n = 7). Vertical lines on the paired mean difference plots indicate 95% bootstrap confidence intervals, and gray histograms show the expected distribution of paired mean differences based on bootstrap analysis.

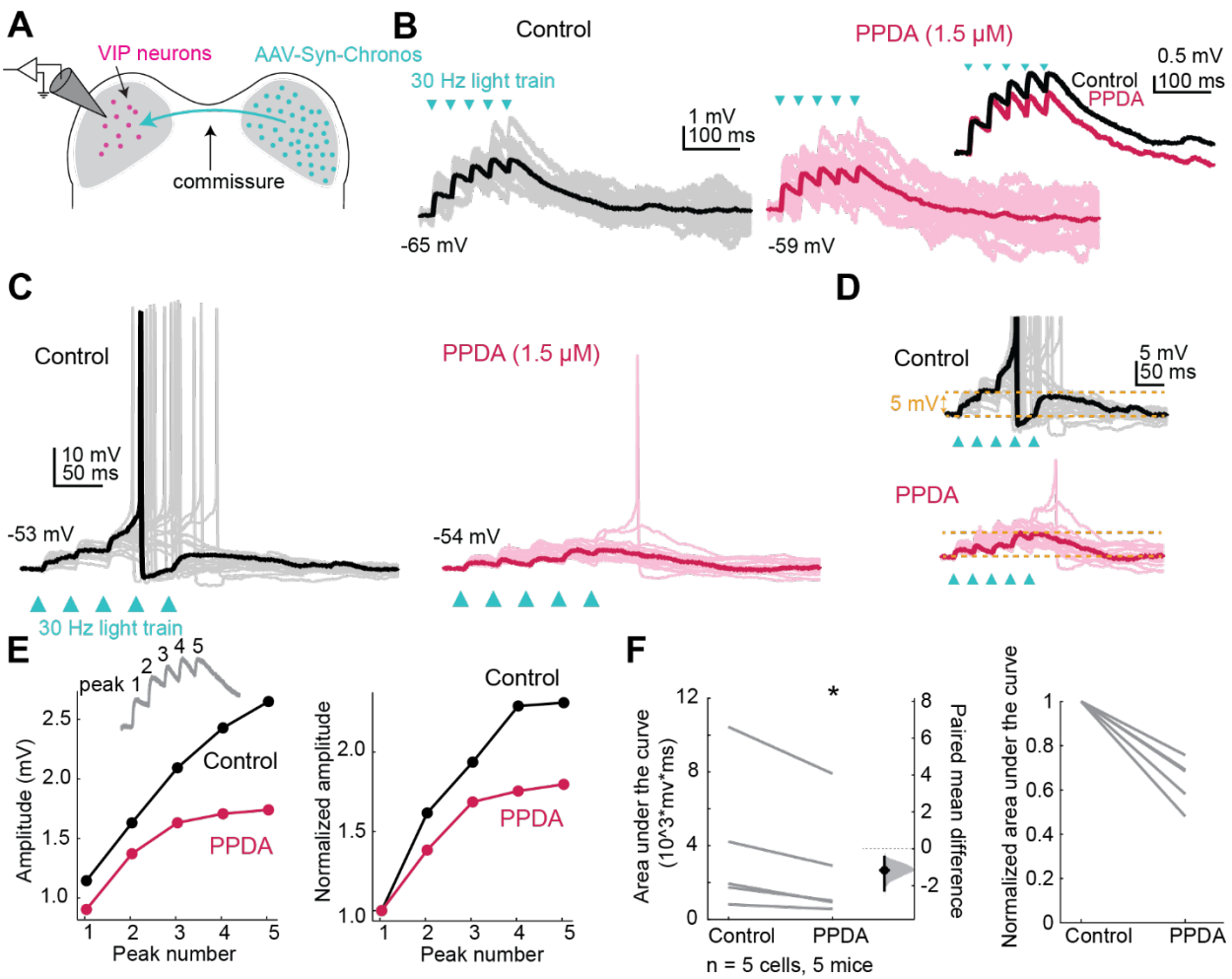

Figure 6. GluN2C/D-containing NMDARs facilitate temporal summation in VIP neurons. ***A,*** Viral injections in the right IC drove Chronos expression in commissural projections to the left IC. Trains of optogenetic stimuli combined with pharmacology were used to examine the contributions of GluN2C/D-containing receptors to temporal summation. ***B,*** EPSP summation elicited by a 30 Hz train of light pulses (left) was decreased by application of the GluN2C/D-specific antagonist PPDA (right, comparison inset). ***C,*** Example of a cell in which summation of optogenetically elicited EPSPs reached action potential threshold, eliciting trains of action potentials. PPDA eliminated spiking in all but one sweep in this cell. ***D,*** Example traces from ***C*** scaled to demonstrate the differences in temporal summation between control and PPDA conditions. ***E,*** The peak amplitude of each EPSP was calculated from the baseline (see inset). The amplitude of the response increased with increasing peak number (LMM: β = 1.06, 95% CI [0.66, 1.47], p = 9.15e-6, n = 5), although the interaction between peak and drug condition was

not statistically significant (β = -0.48, 95% CI [-1.06, 0.095], p = 0.11, n = 5). ***F,*** PPDA significantly decreased the area under the curve for the train of EPSPs (LMM: β = -116.57, 95% CI [-198.93, -34.21], p = 0.038, n = 5), which can be seen in both the non-normalized (left) and normalized (right) plots. Vertical lines on the paired mean difference plots indicate 95% bootstrap confidence intervals, and gray histograms show the expected distribution of paired mean differences based on bootstrap analysis.

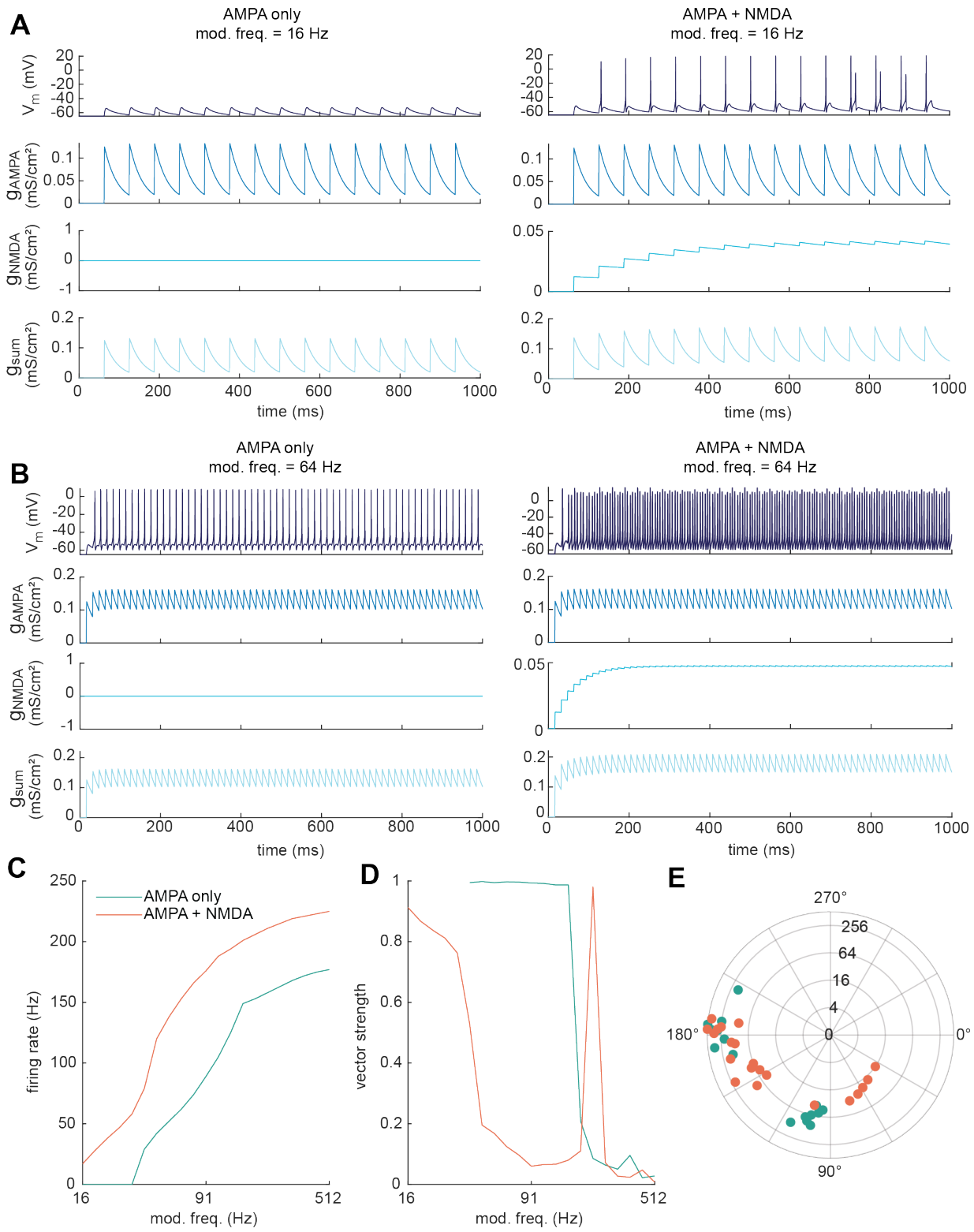

Figure 7. GluN2C/D-like NMDA conductance provides additive gain for rate coding in model IC neuron

866 ***A,*** Model neuron response to a 1 second, 16 Hz input train when the synapse contains an AMPA
867 conductance (left panel) or both AMPA and NMDA conductances (right panel). To mimic
868 GluN2C/D-containing NMDA receptors, the NMDA conductance was not voltage dependent. ***B,***
869 Model neuron response to a 1 second, 64 Hz input train when the synapse contains an AMPA
870 conductance (left panel) or both AMPA and NMDA conductances (right panel). ***C,*** Rate
871 modulation transfer functions for modulation frequencies ranging between 16 – 512 Hz at 4
872 steps/octave. Addition of the NMDA conductance (AMPA + NMDA, orange line) increased the
873 firing rate at all modulation frequencies tested compared to the AMPA conductance alone
874 condition (blue line). ***D,*** Temporal modulation transfer functions in response to the same
875 modulation frequencies shown in ***C***. The model neuron exhibited strong phase locking over the
876 mid-range of input frequencies in the AMPA only condition (blue line), and poorer phase
877 locking in the AMPA plus NMDA condition (orange line). Note that the spike in phase locking at
878 215 Hz for the AMPA plus NMDA condition reflects instance where the sustained firing rate of
879 the model neuron happened to align well with the input frequency. ***E,*** Distribution of firing
880 phases for the AMPA conductance alone (blue dots) and the AMPA plus NMDA conductance
881 (orange dots) conditions. Each dot represents a single modulation frequency. Concentric circles
882 on the polar plot indicate modulation frequency.

883

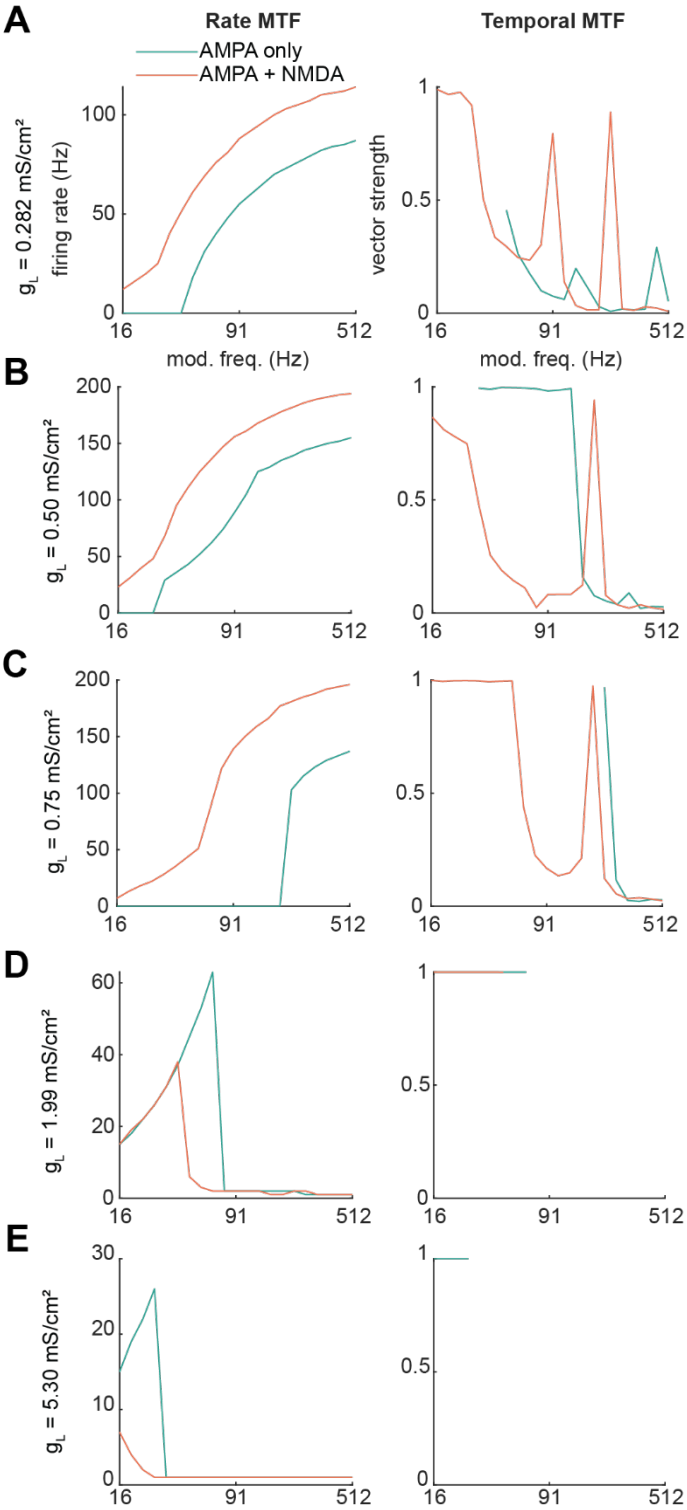

Figure 8. GluN2C/D-like NMDA conductance interacts with membrane resistance and AMPA conductance to shift temporal and rate coding for trains of inputs in the neuron model

887 Model neuron rate and temporal modulation transfer functions for leak conductances of ***A,***
888 0.282, ***B,*** 0.50, ***C,*** 0.75, ***D,*** 1.99, and ***E,*** 5.30 mS/cm^2. For a spherical neuron with a 15 µm
889 diameter, these leak conductances correspond to 502, 283, 189, 71, and 27 MΩ membrane
890 resistances, respectively. Blue lines indicate responses of the model neuron in the AMPA
891 conductance alone condition, while orange lines indicate responses when the model synapse
892 contained both AMPA and NMDA conductances.

893

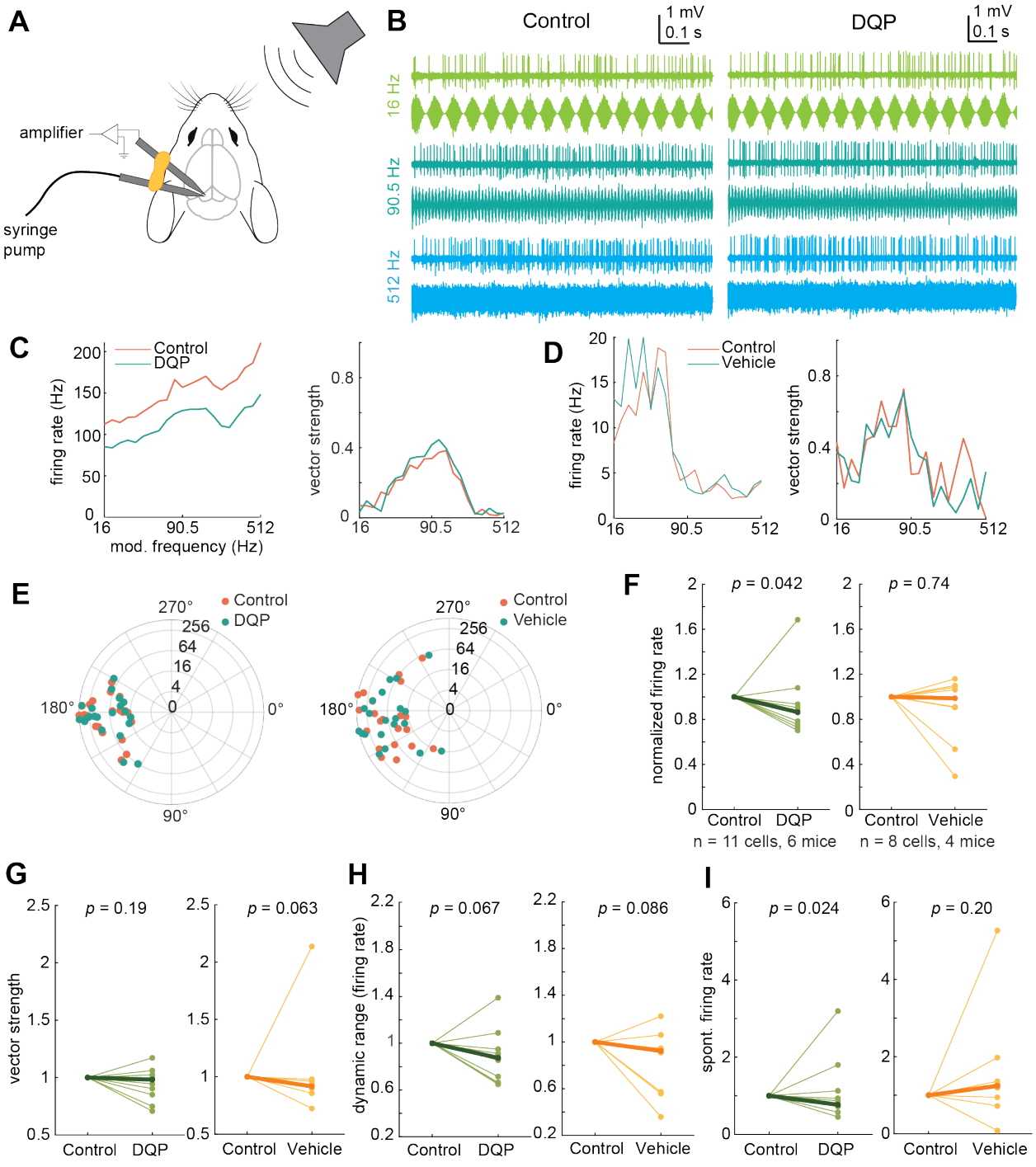

Figure 9. GluN2C/D-containing NMDARs enhance sound-evoked and spontaneous firing rates in vivo

A, Schematic of in vivo recording setup. Adapted from (Petrucco, 2020). In vivo juxtacellular recordings were performed in the IC of awake, headfixed mice using glass electrodes, and DQP

899 or vehicle solution was infused using a piggyback pipette connected to a syringe pump. ***B,***
900 Juxtacellular recordings show both rate and temporal coding of the modulation frequency for
901 AM noise bursts. In this example cell, the firing rate of the neuron increased with increasing
902 modulation frequency. Second panel, the response of the same cell after infusion of the
903 GluN2C/D-specific antagonist DQP. ***C,*** Blocking GluN2C/D-containing NMDA receptors via
904 infusion of DQP decreased the firing rate of the example neuron from ***B*** at all modulation
905 frequencies tested (blue line, left panel). Application of DQP had minimal or no effect on the
906 vector strength of the response at any modulation frequency (right panel). ***D,*** Infusion of
907 vehicle solution into the IC did not alter the firing rate (left panel) or vector strength (right
908 panel) of the response to AM noise bursts. ***E,*** Infusion of DQP (left panel) or vehicle (right panel)
909 did not alter the phases at which firing was phase locked in one DQP example neuron and one
910 vehicle example neuron (orange is pre-infusion, blue is post-infusion). Each dot represents a
911 single modulation frequency. Concentric circles on the polar plot indicate modulation
912 frequency. ***F,*** DQP significantly decreased the number of spikes elicited during the sound
913 stimulus (left panel, Z = 56, p = 0.042, median difference = -1.11 Hz, while vehicle infusion did
914 not change the spike counts (right panel, Z = 21, p = 0.74, median difference = -0.062 Hz). ***G,***
915 DQP infusion (left panel) did not change the average vector strength of the response to AM
916 stimuli (Z = 41, p = 0.19, median difference = -0.008), and vehicle infusion (right panel) also did
917 not affect vector strength (Z = 15, p = 0.063, median difference = -0.018). ***H,*** Infusion of DQP
918 (left panel) did not change the dynamic range of the firing rates over which IC neurons encoded
919 AM modulation frequency (Z = 54, p = 0.067, median difference = -0.13 Hz), and this was also
920 not altered by infusion of vehicle solution (right panel) (Z = 30.5, p = 0.086, median difference =
921 -0.11 Hz). ***I,*** DQP decreased the overall spontaneous firing rate of IC neurons between stimulus
922 presentations (left panel, Z = 58, p = 0.024, median difference = -3.03 Hz), while vehicle infusion
923 had no effect on spontaneous firing rate (right panel, Z = 8, p = 0.20, median difference = 0.76
924 Hz).

925 **Table 1.** Percentage of *tdTomato+* neurons expressing *Glun2d* and/or *Glun2c* mRNA.

Animal	**Slice (n)**	**No. of *tdT+***	**No. of *Glun2d+***	**No. of *Glun2c+***	**No. of *tdT+ Glun2d+ Glun2c+***	**% *tdT+ Glun2d+***	**% *tdT+ Glun2c+***	**% *tdT+ Glun2d+ GluN2c+***
Mouse 1	A caudal	42	36	3	3	85.7%	7.1%	7.1%
	B caudal	52	49	4	4	94.2%	7.7%	7.7%
	C caudal	48	47	2	2	97.9%	4.2%	4.2%
	D rostral	3	3	0	0	100.0%	0.0%	0.0%
	E rostral	4	4	0	0	100.0%	0.0%	0.0%
	Total	**149**	**139**	**9**	**9**	**93.3%**	**6.0%**	**6.0%**
Mouse 2	D caudal	71	68	9	9	95.8%	12.7%	12.7%
	B medial	13	10	2	1	76.9%	15.4%	7.7%
	C medial	26	26	4	4	100.0%	15.4%	15.4%
	A rostral	3	3	0	0	100.0%	0.0%	0.0%
	Total	**113**	**107**	**15**	**14**	**94.7%**	**13.3%**	**12.4%**
Mouse 3	B caudal	94	83	10	7	88.3%	10.6%	7.4%
	D caudal	85	76	5	5	89.4%	5.9%	5.9%
	A medial	70	62	2	1	88.6%	2.9%	1.4%
	C rostral	10	9	1	1	90.0%	10.0%	10.0%
	Total	**259**	**230**	**18**	**14**	**88.8%**	**6.9%**	**5.4%**
Grand total		**521**	**476**	**42**	**37**	**91.4%**	**8.1%**	**7.1%**

926

927 **Table 1.**

928 The number and percentage of *tdTomato* positive cells that expressed *Glun2c* and *Glun2d*
929 mRNA using an RNAScope in situ hybridization assay. Data is from a series of coronal IC sections
930 collected from three VIP-IRES-Cre x Ai14 mice aged P45-47.

931 **Table 2.** Percentage of neurons that expressed *Glun2d* and *Glun2c* in IC central nucleus, dorsal
932 cortex, and lateral cortex

Location	Mouse	No. of *tdT+*	No. of *Glun2d+*	No. of *Glun2c+*	No. of *tdT+ Glun2d+ Glun2c+*	% *tdT+ Glun2d+*	% *tdT+ Glun2c+*	% *tdT+ Glun2d+ Glun2c+*
Central nucleus	1	89	84	5	5	94.4%	5.6%	5.6%
	2	68	67	12	12	98.5%	17.6%	17.6%
	3	199	175	14	11	87.9%	7.0%	5.5%
	Total	**356**	**326**	**31**	**28**	**91.6%**	**8.7%**	**7.9%**
Dorsal cortex	1	47	42	4	4	89.4%	8.5%	8.5%
	2	28	25	1	1	89.3%	3.6%	3.6%
	3	38	36	2	2	94.7%	5.3%	5.3%
	Total	**113**	**103**	**7**	**7**	**91.2%**	**6.2%**	**6.2%**
Lateral cortex	1	13	13	0	0	100.0%	0.0%	0.0%
	2	17	15	2	1	88.2%	11.8%	5.9%
	3	22	19	2	1	86.4%	9.1%	4.5%
	Total	**52**	**47**	**4**	**2**	**90.4%**	**7.7%**	**3.8%**
Grand total		**521**	**476**	**42**	**37**	**91.4%**	**8.1%**	**7.1%**

933

934 **Table 2.**

935 The number and percentage of *tdTomato* positive cells in the three major IC subdivisions
936 (central nucleus, lateral cortex, and dorsal cortex) that expressed *Glun2c* and *Glun2d* mRNA
937 using an RNAScope in situ hybridization assay. Data is from a series of coronal IC sections
938 collected from three VIP-IRES-Cre x Ai14 mice aged P45-47.

939 **References**

940 Adams JC (1979) Ascending projections to the inferior colliculus. J Comp Neurol 183:519–538.

941 Anair JD, Silveira MA, Mirjalili P, Beebe NL, Schofield BR, Roberts MT (2022) Inhibitory NPY
942 Neurons Provide a Large and Heterotopic Commissural Projection in the Inferior
943 Colliculus. Front Neural Circuits 16:871924.

944 Bates D, Mächler M, Bolker B, Walker S (2015) Fitting Linear Mixed-Effects Models Using lme4. J
945 Stat Softw 67:1–48.

946 Beebe NL, Schofield BR (2021) Cholinergic boutons are closely associated with excitatory cells
947 and four subtypes of inhibitory cells in the inferior colliculus. J Chem Neuroanat
948 116:101998.

949 Beebe NL, Silveira MA, Goyer D, Noftz WA, Roberts MT, Schofield BR (2022) Neurotransmitter
950 phenotype and axonal projection patterns of VIP-expressing neurons in the inferior
951 colliculus. J Chem Neuroanat 126:102189.

952 Bernard C (2019) Changing the Way We Report, Interpret, and Discuss Our Results to Rebuild
953 Trust in Our Research. eNeuro 6:ENEURO.0259-19.2019.

954 Binshtok AM, Fleidervish IA, Sprengel R, Gutnick MJ (2006) NMDA receptors in layer 4 spiny
955 stellate cells of the mouse barrel cortex contain the NR2C subunit. J Neurosci 26:708–
956 715.

957 Börgers, Christoph (2017) An Introduction to Modeling Neuronal Dynamics. In: An Introduction
958 to Modeling Neuronal Dynamics, 1st ed., pp 153–192 Texts in Applied Mathematics.
959 Springer International Publishing.

960 Brickley SG, Misra C, Mok MHS, Mishina M, Cull-Candy SG (2003) NR2B and NR2D subunits
961 coassemble in cerebellar Golgi cells to form a distinct NMDA receptor subtype restricted
962 to extrasynaptic sites. J Neurosci Off J Soc Neurosci 23:4958–4966.

963 Brothwell SLC, Barber JL, Monaghan DT, Jane DE, Gibb AJ, Jones S (2008) NR2B- and NR2D-
964 containing synaptic NMDA receptors in developing rat substantia nigra pars compacta
965 dopaminergic neurones. J Physiol 586:739–750.

966 Calin-Jageman RJ, Cumming G (2019) Estimation for Better Inference in Neuroscience. eNeuro
967 6:ENEURO.0205-19.2019.

968 Choy Buentello D, Bishop DC, Oliver DL (2015) Differential distribution of GABA and glycine
969 terminals in the inferior colliculus of rat and mouse. J Comp Neurol 523:2683–2697.

970 D'Angelo E, De Filippi G, Rossi P, Taglietti V (1995) Synaptic excitation of individual rat
971 cerebellar granule cells in situ: evidence for the role of NMDA receptors. J Physiol 484 (
972 Pt 2):397–413.

973 Drotos AC, Roberts MT (2024) Identifying neuron types and circuit mechanisms in the auditory
974 midbrain. Hear Res 442:108938.

975 Feng Z-J, Zhang X, Chergui K (2014) Allosteric modulation of NMDA receptors alters
976 neurotransmission in the striatum of a mouse model of Parkinson's disease. Exp Neurol
977 255:154–160.

978 Forman CJ, Tomes H, Mbobo B, Burman RJ, Jacobs M, Baden T, Raimondo JV (2017)
979 Openspritzer: an open hardware pressure ejection system for reliably delivering picolitre
980 volumes. Sci Rep 7:2188.

981 Geis H-R, Borst JGG (2009) Intracellular responses of neurons in the mouse inferior colliculus to
982 sinusoidal amplitude-modulated tones. J Neurophysiol 101:2002–2016.

983 Goyer D, Silveira MA, George AP, Beebe NL, Edelbrock RM, Malinski PT, Schofield BR, Roberts
984 MT (2019) A novel class of inferior colliculus principal neurons labeled in vasoactive
985 intestinal peptide-Cre mice. eLife 8:32.

986 Groc L, Heine M, Cousins SL, Stephenson FA, Lounis B, Cognet L, Choquet D (2006) NMDA
987 receptor surface mobility depends on NR2A-2B subunits. Proc Natl Acad Sci U S A
988 103:18769–18774.

989 Harney SC, Jane DE, Anwyl R (2008) Extrasynaptic NR2D-containing NMDARs are recruited to
990 the synapse during LTP of NMDAR-EPSCs. J Neurosci Off J Soc Neurosci 28:11685–11694.

991 Hewitt MJ, Meddis R (1994) A computer model of amplitude-modulation sensitivity of single
992 units in the inferior colliculus. J Acoust Soc Am 95:2145–2159.

993 Hildebrand ME, Pitcher GM, Harding EK, Li H, Beggs S, Salter MW (2014) GluN2B and GluN2D
994 NMDARs dominate synaptic responses in the adult spinal cord. Sci Rep 4:4094.

995 Ho J, Tumkaya T, Aryal S, Choi H, Claridge-Chang A (2019) Moving beyond P values: data
996 analysis with estimation graphics. Nat Methods 16:565–566.

997 Hodgkin AL, Huxley AF (1952) A quantitative description of membrane current and its
998 application to conduction and excitation in nerve. J Physiol 117:500–544.

999 Hosomi H, Hirai H, Okadaa Y, Amatsu M (1995) Long-term potentiation of neurotransmission in
1000 the inferior colliculus of the rat. Neurosci Lett 195:175–178.

1001 Huang Z, Gibb AJ (2014) Mg2+ block properties of triheteromeric GluN1-GluN2B-GluN2D NMDA
1002 receptors on neonatal rat substantia nigra pars compacta dopaminergic neurones. J
1003 Physiol 592:2059–2078.

1004 Hunt DL, Castillo PE (2012) Synaptic plasticity of NMDA receptors: mechanisms and functional
1005 implications. Curr Opin Neurobiol 22:496–508.

1006 Jing P-B, Chen X-H, Lu H-J, Gao Y-J, Wu X-B (2022) Enhanced function of NR2C/2D-containing
1007 NMDA receptor in the nucleus accumbens contributes to peripheral nerve injury-
1008 induced neuropathic pain and depression in mice. Mol Pain 18:17448069211053256.

1009 Joris PX, Schreiner CE, Rees A (2004) Neural processing of amplitude-modulated sounds. Physiol
1010 Rev 84:541–577.

1011 Kay M (2024) ggdist: Visualizations of Distributions and Uncertainty in the Grammar of
1012 Graphics. IEEE Trans Vis Comput Graph 30:414–424.

1013 Kelly JB, Zhang H (2002) Contribution of AMPA and NMDA receptors to excitatory responses in
1014 the inferior colliculus. Hear Res 168:35–42.

1015 Kim DO, Carney LH, Kuwada S (2020) Amplitude modulation transfer functions reveal opposing
1016 populations within both the inferior colliculus and medial geniculate body. J
1017 Neurophysiol Available at: http://dx.doi.org/10.1152/jn.00279.2020.

1018 Klapoetke NC et al. (2014) Independent optical excitation of distinct neural populations. Nat
1019 Methods 11:338–346.

1020 Krishna BS, Semple MN (2000) Auditory Temporal Processing: Responses to Sinusoidally
1021 Amplitude-Modulated Tones in the Inferior Colliculus. J Neurophysiol 84:255–273.

1022 Kumar SS, Huguenard JR (2003) Pathway-specific differences in subunit composition of synaptic
1023 NMDA receptors on pyramidal neurons in neocortex. J Neurosci Off J Soc Neurosci
1024 23:10074–10083.

1025 Kuznetsova A, Brockhoff PB, Christensen RHB (2017) lmerTest Package: Tests in Linear Mixed
1026 Effects Models. J Stat Softw 82:1–26.

1027 Li Y-H, Li Y, Zheng L, Wang J (2020) Postsynaptic GluN2B-containing NMDA receptors contribute
1028 to long-term depression induction in medial vestibular nucleus neurons of juvenile rats.
1029 Neurosci Lett 715:134674.

1030 Liu J, Shelkar GP, Sarode LP, Gawande DY, Zhao F, Clausen RP, Ugale RR, Dravid SM (2021)
1031 Facilitation of GluN2C-containing NMDA receptors in the external globus pallidus
1032 increases firing of fast spiking neurons and improves motor function in a
1033 hemiparkinsonian mouse model. Neurobiol Dis 150:105254.

1034 Lo F-S, Akkentli F, Tsytsarev V, Erzurumlu RS (2013) Functional significance of cortical NMDA
1035 receptors in somatosensory information processing. J Neurophysiol 110:2627–2636.

1036 Logan SM, Partridge JG, Matta JA, Buonanno A, Vicini S (2007) Long-lasting NMDA receptor-
1037 mediated EPSCs in mouse striatal medium spiny neurons. J Neurophysiol 98:2693–2704.

1038 Lozovaya NA, Grebenyuk SE, Tsintsadze TS, Feng B, Monaghan DT, Krishtal OA (2004)
1039 Extrasynaptic NR2B and NR2D subunits of NMDA receptors shape "superslow"
1040 afterburst EPSC in rat hippocampus. J Physiol 558:451–463.

1041 Ma CL, Kelly JB, Wu SH (2002) AMPA and NMDA receptors mediate synaptic excitation in the
1042 rat's inferior colliculus. Hear Res 168:25–34.

1043 Madisen L, Zwingman TA, Sunkin SM, Oh SW, Zariwala HA, Gu H, Ng LL, Palmiter RD, Hawrylycz
1044 MJ, Jones AR, Lein ES, Zeng H (2010) A robust and high-throughput Cre reporting and
1045 characterization system for the whole mouse brain. Nat Neurosci 13:133–140.

1046 Malenka RC, Nicoll RA (1993) NMDA-receptor-dependent synaptic plasticity: multiple forms and
1047 mechanisms. Trends Neurosci 16:521–527.

1048 Misra C, Brickley SG, Farrant M, Cull-Candy SG (2000) Identification of subunits contributing to
1049 synaptic and extrasynaptic NMDA receptors in Golgi cells of the rat cerebellum. J Physiol
1050 524 Pt 1:147–162.

1051 Momiyama A (2000) Distinct synaptic and extrasynaptic NMDA receptors identified in dorsal
1052 horn neurones of the adult rat spinal cord. J Physiol 523 Pt 3:621–628.

1053 Monyer H, Burnashev N, Laurie DJ, Sakmann B, Seeburg PH (1994) Developmental and regional
1054 expression in the rat brain and functional properties of four NMDA receptors. Neuron
1055 12:529–540.

1056 Monyer H, Sprengel R, Schoepfer R, Herb A, Higuchi M, Lomeli H, Burnashev N, Sakmann B,
1057 Seeburg PH (1992) Heteromeric NMDA receptors: molecular and functional distinction
1058 of subtypes. Science 256:1217–1221.

1059 Mullasseril P, Hansen KB, Vance KM, Ogden KK, Yuan H, Kurtkaya NL, Santangelo R, Orr AG, Le
1060 P, Vellano KM, Liotta DC, Traynelis SF (2010) A subunit-selective potentiator of NR2C-
1061 and NR2D-containing NMDA receptors. Nat Commun 1:90.

1062 Nelson PC, Carney LH (2007) Neural Rate and Timing Cues for Detection and Discrimination of
1063 Amplitude-Modulated Tones in the Awake Rabbit Inferior Colliculus. J Neurophysiol
1064 97:522–539.

1065 Nouhi M, Zhang X, Yao N, Chergui K (2018) CIQ, a positive allosteric modulator of GluN2C/D-
1066 containing N-methyl-d-aspartate receptors, rescues striatal synaptic plasticity deficit in a
1067 mouse model of Parkinson's disease. CNS Neurosci Ther 24:144–153.

1068 Oberle HM, Ford AN, Dileepkumar D, Czarny J, Apostolides PF (2022) Synaptic mechanisms of
1069 top-down control in the non-lemniscal inferior colliculus. eLife 10:e72730.

1070 Oliver DL, Huerta MF (1992) Inferior and Superior Colliculi. In: The Mammalian Auditory
1071 Pathway: Neuroanatomy (Webster DB, Popper AN, Fay RR, eds), pp 168–221. New York,
1072 NY: Springer New York.

1073 Paoletti P, Bellone C, Zhou Q (2013) NMDA receptor subunit diversity: impact on receptor
1074 properties, synaptic plasticity and disease. Nat Rev Neurosci 14:383–400.

1075 Petrucco L (2020) Mouse head schema. Available at: https://zenodo.org/records/3925903
1076 [Accessed April 15, 2024].

1077 Rebola N, Srikumar BN, Mulle C (2010) Activity-dependent synaptic plasticity of NMDA
1078 receptors. J Physiol 588:93–99.

1079 Rees A, Møller AR (1983) Responses of neurons in the inferior colliculus of the rat to AM and
1080 FM tones. Hear Res 10:301–330.

1081 Rees A, Palmer AR (1989) Neuronal responses to amplitude-modulated and pure-tone stimuli in
1082 the guinea pig inferior colliculus, and their modification by broadband noise. J Acoust
1083 Soc Am 85:1978–1994.

1084 Rhode WS, Greenberg S (1994) Encoding of amplitude modulation in the cochlear nucleus of
1085 the cat. J Neurophysiol 71:1797–1825.

1086 Rivera-Perez LM, Kwapiszewski JT, Roberts MT (2021) α3β4 ∗ Nicotinic Acetylcholine Receptors
1087 Strongly Modulate the Excitability of VIP Neurons in the Mouse Inferior Colliculus. Front
1088 Neural Circuits 15:709387.

1089 Shravan Vasishth, Daniel Shad, Audrey Bürki, Reinhold Kliegl (2022) From the t-test to the linear
1090 (mixed) model. In: Linear Mixed Models in Linguistics and Psychology: A Comprehensive
1091 Introduction Available at: https://vasishth.github.io/Freq_CogSci/.

1092 Siegler Retchless B, Gao W, Johnson JW (2012) A single GluN2 subunit residue controls NMDA
1093 receptor channel properties via intersubunit interaction. Nat Neurosci 15:406–413, S1-2.

1094 Silveira MA, Anair JD, Beebe NL, Mirjalili P, Schofield BR, Roberts MT (2020) Neuropeptide Y
1095 Expression Defines a Novel Class of GABAergic Projection Neuron in the Inferior
1096 Colliculus. J Neurosci 40:4685–4699.

1097 Silver RA (2010) Neuronal arithmetic. Nat Rev Neurosci 11:474–489.

1098 Taniguchi H, He M, Wu P, Kim S, Paik R, Sugino K, Kvitsani D, Fu Y, Lu J, Lin Y, Miyoshi G, Shima
1099 Y, Fishell G, Nelson SB, Huang ZJ (2011) A Resource of Cre Driver Lines for Genetic
1100 Targeting of GABAergic Neurons in Cerebral Cortex. Neuron 71:995–1013.

1101 Tovar KR, Westbrook GL (2002) Mobile NMDA receptors at hippocampal synapses. Neuron
1102 34:255–264.

1103 Traynelis SF, Wollmuth LP, McBain CJ, Menniti FS, Vance KM, Ogden KK, Hansen KB, Yuan H,
1104 Myers SJ, Dingledine R (2010) Glutamate Receptor Ion Channels: Structure, Regulation,
1105 and Function Sibley D, ed. Pharmacol Rev 62:405–496.

1106 Vicini S, Wang JF, Li JH, Zhu WJ, Wang YH, Luo JH, Wolfe BB, Grayson DR (1998) Functional and
1107 pharmacological differences between recombinant N-methyl-D-aspartate receptors. J
1108 Neurophysiol 79:555–566.

1109 Wang F, Flanagan J, Su N, Wang L-C, Bui S, Nielson A, Wu X, Vo H-T, Ma X-J, Luo Y (2012)
1110 RNAscope: a novel in situ RNA analysis platform for formalin-fixed, paraffin-embedded
1111 tissues. J Mol Diagn JMD 14:22–29.

1112 Wang XJ, Buzsáki G (1996) Gamma oscillation by synaptic inhibition in a hippocampal
1113 interneuronal network model. J Neurosci Off J Soc Neurosci 16:6402–6413.

1114 Wenzel A, Villa M, Mohler H, Benke D (1996) Developmental and regional expression of NMDA
1115 receptor subtypes containing the NR2D subunit in rat brain. J Neurochem 66:1240–
1116 1248.

1117 Wu SH (2004) Contribution of AMPA, NMDA, and GABAA Receptors to Temporal Pattern of
1118 Postsynaptic Responses in the Inferior Colliculus of the Rat. J Neurosci 24:4625–4634.

1119 Wu SH, Ma CL, Sivaramakrishnan S, Oliver DL (2002) Synaptic modification in neurons of the
1120 central nucleus of the inferior colliculus. Hear Res 168:43–54.

1121 Yi F, Bhattacharya S, Thompson CM, Traynelis SF, Hansen KB (2019) Functional and
1122 pharmacological properties of triheteromeric GluN1/2B/2D NMDA receptors. J Physiol
1123 597:5495–5514.

1124 Yin P, Johnson JS, O'Connor KN, Sutter ML (2011) Coding of Amplitude Modulation in Primary
1125 Auditory Cortex. J Neurophysiol 105:582–600.

1126 Zhang H, Kelly JB (2001) AMPA and NMDA Receptors Regulate Responses of Neurons in the
1127 Rat's Inferior Colliculus. J Neurophysiol 86:871–880.

1128 Zhang X, Feng Z-J, Chergui K (2014) Allosteric modulation of GluN2C/GluN2D-containing NMDA
1129 receptors bidirectionally modulates dopamine release: implication for Parkinson's
1130 disease. Br J Pharmacol 171:3938–3945.

1131 Zhang Y, Wu SH (2000) Long-term potentiation in the inferior colliculus studied in rat brain slice.
1132 Hear Res 147:92–103.

1133 Zheng QY, Johnson KR, Erway LC (1999) Assessment of hearing in 80 inbred strains of mice by
1134 ABR threshold analyses. Hear Res 130:94–107.

1135